

Signatures of Young Planets in the Continuum Emission From Protostellar Disks

Andrea Isella

*Department of Physics and Astronomy, Rice University
6100 Main Street, MS-108, Houston, Texas 77005*

`isella@rice.edu`

and

Neal J. Turner

*Jet Propulsion Laboratory, California Institute of Technology
4800 Oak Grove Drive, Pasadena, California 91109*

`neal.turner@jpl.nasa.gov`

ABSTRACT

Many protostellar disks show central cavities, rings, or spiral arms that could be caused by low-mass stellar or planetary companions. Few of these features are yet conclusively tied to objects embedded in the disks, perhaps because of shortcomings in our understanding of what a disk interacting with a planet looks like at the wavelengths we observe. We approach these issues noting that even small features on the disk’s surface cast shadows, because the starlight grazes the surface at low angles. We therefore focus on accurately computing the disk’s thickness, and thus its temperature. We present models that are in hydrostatic equilibrium in the vertical direction, with temperatures set by the balance between starlight heating and radiative cooling. The embedded planet has 20, 100, or 1000 M_{\oplus} , ranging from barely enough to perturb the disk gas surface density significantly, to able to clear a deep tidal gap. Two-dimensional hydrodynamical calculations in the equatorial plane yield surface density maps, which we expand into three-dimensional density distributions using the hydrostatic equilibrium for the initially guessed temperature distribution. We compute new temperatures using detailed frequency-dependent Monte Carlo radiative transfer calculations treating scattering, absorption and thermal re-emission. We then step forward in time, letting each patch of the disk expand or contract vertically on its own thermal or dynamical timescale, and again compute temperatures accounting for the way the starlight falls across the disk’s new shape. The calculations continue as long as needed to reach joint

radiative and hydrostatic equilibrium. The hydrostatic balance makes a striking difference to the model disk’s appearance. The planet-carved gap’s outer wall receives extra starlight heating and puffs up, throwing a shadow across the disk beyond. The shadow appears in scattered light as an additional dark ring, which could be mistaken for a gap opened by another more distant planet. Our model with the $100\text{-}M_{\oplus}$ planet has the surface brightness contrast between outer wall and shadow almost an order of magnitude greater than a version neglecting the temperature disturbances caused by the planet. The shadow is so deep it largely hides the outer arm of the spiral wave launched by the planet. The massive planets yield temperature gradients such that additional more distant low-mass planets undergoing orbital migration will converge on a location within the shadow. Furthermore the temperature perturbations affect the shape, size and contrast of the features predicted at millimeter and centimeter wavelengths. We conclude that radiative heating and cooling are important ingredients for reliably predicting the appearance of protostellar disks with embedded planets.

Subject headings: protostellar disks — hydrodynamics — radiative transfer

1. Introduction

Extrasolar planetary systems are now known to be strikingly diverse in the member planets’ masses, multiplicities and orbital configurations (Udry & Santos 2007; Batalha et al. 2013; Laughlin & Lissauer 2015; Winn & Fabrycky 2015). Placing our Solar system in the context of these new discoveries will require learning how the diversity arises from differing conditions or processes in the protostellar disks that gave the planets birth. A promising way forward is by studying spatially resolved observations of the protostellar disks orbiting nearby young stars, which reveal numerous features in the emission from the dust and gas: central cavities, bright and dark rings, including asymmetric ones, and spiral arms. These features are qualitatively consistent with gravitational perturbation by low-mass stellar or planetary companions, and offer an opportunity to learn about the early stages of planet and star formation within the disks.

Clear examples of the variety of structures found in protostellar disks are around the young stars SAO 206462, MWC 758, J160421.7-213028 (hereafter J1604) and LkCa 15. All four disks have large cavities that are dark in the continuum emission from millimeter and centimeter-size grains. While the first two show horseshoe-shaped azimuthal asymmetries (Pérez et al. 2014a; Isella et al. 2010), the latter two are almost axisymmetric at millimeter wavelengths (Zhang et al. 2014; Isella et al. 2012). In the optical and near-infrared, the SAO 206462 disk shows a well-defined $m = 2$ spiral design (Muto et al. 2012), while MWC 758 has a single spiral arm and a circular arc (Benisty et al. 2015). In contrast, the infrared surface brightness around both J1604 and LkCa 15 is circularly symmetric (Mayama et al. 2012a; Thalmann et al. 2010), similar in shape to the millimeter wavelengths.

The dynamical interaction between the circumstellar material and planets or low-mass stellar companions is the most widely accepted explanation for the observed structures. This is because, on one hand, circular gaps, spiral waves, and azimuthal asymmetries are naturally produced by the gravitational interaction with one or more companions (Baruteau et al. 2014; Kley & Nelson 2012), and on the other hand, the search for exoplanets has revealed that most mature stars host one or more planets, therefore many protostellar disks should show the effects of planet formation.

Recent observations however point to major discrepancies with planet-disk interaction models. For example, the infrared spiral arm observed in the MWC 758 disk has large opening angles, which, if interpreted as the manifestation of density waves propagating away from an embedded planet at the local sound speed, implies temperatures much higher than equilibrium with the stellar radiation field (Benisty et al. 2015). Furthermore, Juhász et al. (2015) pointed out that the appearance of the spiral structures in scattered light requires disk pressure scale heights several times larger than expected under hydrostatic equilibrium. Finally, some models used to interpret the observed spiral features lack internal consistency. As an example, planet masses of several Jupiters were derived in the case of SAO 206462 by adopting prescriptions for the disk-planet interaction that hold only for planets with masses less than 1 Earth. In contrast, the rather simple morphologies of the LkCa 15 and J1604 disks, and even the multi-ring morphology in HL Tau, can be explained using planet-disk interaction models (Jin et al. 2016; Dong et al. 2015c; Picogna & Kley 2015; Pinilla et al. 2015; Jang-Condell & Turner 2013). Furthermore, a young planet has been imaged in the dust-depleted cavity of LkCa 15 (Sallum et al. 2015). Based on this sample, we might argue that the features in “dynamically cold” disks such as J1604 and LkCa 15 result from planet-disk interaction, while those in “dynamically hot” disks such as SAO 206462 and MWC 758 come from other yet unknown physical processes.

Improving our understanding of planet-disk interaction requires both enlarging the still small and biased sample of disks observed at high angular resolution, and improving upon theoretical models of the disks’ response to perturbations from stellar and planetary companions. In this paper we address the modeling issue, motivated by the fact that current treatments of embedded planets’ effects on the disk’s appearance involve very simple prescriptions for the disk’s thermal response. Juhász et al. (2015) noted that spiral structures in the scattered light are more sensitive to disturbances in the disk’s pressure scale height than to disturbances in the density. The scale height is proportional to the sound speed and thus depends on the temperature. The temperature in turn is highly sensitive to the angle of incidence of the starlight, so accurately calculating the shape of the disk surface is crucial for modeling the system’s appearance (Jang-Condell 2008).

To address these issues, we first investigate the planet-disk interaction’s effects on the disk temperature and density. We describe our modeling approach in section 2, and its results in section 3. We find that planets affect the temperatures through the interplay between starlight heating, the disk’s shape, and radiative cooling. We then apply the model to investigate the planet-induced perturbations’ observational appearance. We focus our attention on signatures in infrared scattered light, which trace the disk’s surface layers, and in millimeter-wave dust continuum

emission, which trace the dust in the midplane. Section 4 deals with the temperature structures’ implications for disks’ equation of state and planets’ orbital migration. The models’ relationship to the features observed in protostellar disks is discussed in section 5, and the conclusions are presented in section 6.

2. Modeling the Planet-Disk Interaction

Accurately modeling the planet-disk interaction requires solving the following problem. The orbiting planet exerts a gravitational force on nearby disk material, launching acoustic waves which compress and rarefy the gas through which they pass, perturbing the surface density. The density fluctuations alter the height and slope of the surface where the illuminating starlight is absorbed. Large enough excursions of the surface cast shadows across the disk beyond. The changing illumination is reflected in the system’s appearance in scattered light. Over the heating or cooling timescale, the changing illumination also affects the interior temperatures, which feed back on the acoustic waves’ own propagation. Furthermore, planets more massive than Jupiter launch waves strong enough to clear disk material from an annulus around the planetary orbit. This drastic change in the disk structure further alters how starlight is absorbed and scattered across the disk.

Several approximations are necessary to make this problem tractable. To begin with, we assume that the planet disturbs the disk in a way that depends weakly on the temperature, so we can solve for the gas dynamics using temperatures differing from those we will eventually determine through detailed Monte Carlo radiative transfer. We find that this is valid for planets too low in mass to open a gap in the disk. However the formation of a gap leads to large temperature excursions, making the approximation questionable. We nevertheless separate the dynamics and radiative transfer because the latter takes far too much computer time to be carried out with each hydrodynamical timestep. Frequency-averaged semi-analytic transfer methods are much faster (Jang-Condell 2009) and adequately reproduce the results of detailed transfer calculations (Jang-Condell & Turner 2012), but have not been combined with the 3-D hydrodynamical methods needed to model the surface-illuminated disk’s non-axisymmetric response to an embedded planet. Numerical 3-D radiation hydrodynamics modeling is now feasible in the flux-limited diffusion approximation (Bitsch & Kley 2011), including with the direct illumination treated by integrating along rays from the star (Flock et al. 2013), but the flux-limiting yields wrong answers when shadowing is important (Hayes & Norman 2003), and these approaches neglect scattered starlight. Thus the models for gap-opening planets presented below, despite their limitations, provide insights into the appearance of disks with embedded planets that are not available from other existing results.

2.1. Unperturbed Disk

We start our investigation by adopting a disk model unperturbed by any planet, with gas surface density

$$\Sigma_g^0(r) = 18 \text{ g cm}^{-2} \times \left(\frac{r}{10\text{AU}} \right)^{-1} \quad (1)$$

extending from 0.1 AU to 50 AU. Its total mass is $0.007 M_\odot$, less than the minimum-mass Solar nebula but consistent with the masses of young disks in nearby star forming regions (e.g. Andrews & Williams 2007; Isella et al. 2009).

The central star has a mass of $1 M_\odot$, a luminosity of $1 L_\odot$, and an effective temperature of 5600 K. The disk temperature and vertical density structure are calculated under the assumption of hydrostatic equilibrium between the gas pressure and the stellar gravity. Dust is well-mixed throughout the gas, with a uniform gas-to-dust ratio of 100. The interaction between dust and gas is further discussed in Section 2.3. Temperatures are computed using the Monte Carlo radiative transfer code RADMC-3D. The disk is placed in radiative equilibrium, so that the bolometric emission from each grid cell matches the rate at which starlight and other incident radiation are absorbed, following the procedure discussed in Section 2.4.

The midplane temperature of the resulting unperturbed disk model is well approximated by the power-law fit

$$T_m^0(r) \simeq 37\text{K} \times \left(\frac{r}{10\text{AU}} \right)^{-1/2}. \quad (2)$$

The temperature along the direction perpendicular to the midplane is equal to $T_m^0(r)$ for $z/r < h/r \approx 0.04$. At greater heights the temperature increases to reach that of a dust grain in optically thin surroundings exposed to the starlight, $T_s^0(r) \simeq 124\text{K}(r/10\text{AU})^{-1/2}$ (Dullemond et al. 2001; Dullemond & Dominik 2004, e.g.).

Since most of the disk’s mass lies in the vertically-isothermal interior, the vertical density profile to first approximation is the Gaussian

$$\rho(r, z) = \frac{\Sigma(r)}{\sqrt{2\pi}h(r)} e^{-z^2/2h(r)^2}. \quad (3)$$

At hydrostatic equilibrium, the pressure scale height $h(r)$ is equal to $c_s(r)/\Omega(r)$, where $c_s(r) = \sqrt{\gamma k_b T(r)/\mu m_p}$ is the gas sound speed, and $\Omega(r) = \sqrt{GM_\star/r^3}$ is the Keplerian angular speed. Using the gas temperature from Equation 2, a mean molecular weight $\mu = 2.3$, and an adiabatic index $\gamma = 7/5$ appropriate for molecular hydrogen, the sound speed and pressure scale height are

$$c_s^0(r) \simeq 0.43 \text{ km s}^{-1} \times \left(\frac{r}{10\text{AU}} \right)^{-1/4} \quad (4)$$

and

$$h^0(r) \simeq 0.43\text{AU} \times \left(\frac{r}{10\text{AU}} \right)^{5/4}. \quad (5)$$

Below we use the fits in equations 1-5 as baselines against which to compare the structure of model disks perturbed by planets.

2.2. Planets Perturbing the Disk

The first step in producing synthetic images of a disk interacting with an embedded planet is to map the perturbations in the surface density. If the planet is low-mass, the perturbations are small and can be calculated by linearizing the equations of motion and continuity (Goldreich & Tremaine 1978). In contrast, high-mass planets induce non-linear perturbations that must be investigated using numerical simulations (Bryden et al. 1999). The transition between these two regimes occurs when non-linear effects, such as shocks, become relevant in transferring the angular momentum carried by the waves into the gas (Goodman & Rafikov 2001).

The transition from linear to non-linear perturbations in a Keplerian disk occurs around the thermal mass $M_{th} = 2c_s^3/3\Omega G$ (Goodman & Rafikov 2001; Dong et al. 2011). A planet with mass $M_p = M_{th}$ has a Hill sphere whose radius is comparable to the disk’s pressure scale height. In an inviscid disk, M_{th} is the mass at which planets start to open annular gaps in the surrounding gas by depositing angular momentum at their innermost Lindblad resonance (Lin & Papaloizou 1993).

For the unperturbed disk model described above, the critical mass is

$$M_{th} \sim 20M_{\oplus} \times \left(\frac{r}{10\text{AU}}\right)^{3/4}. \quad (6)$$

If $M_p \ll M_{th}$, the planet perturbation’s waveform can be written in polar coordinates as

$$\phi = \phi_p - \text{sign}(r - r_p) \frac{r_p}{h_p} \times 4 \left[\left(\frac{r}{r_p}\right)^{-1/4} - \frac{1}{5} \left(\frac{r}{r_p}\right)^{5/4} + \frac{6}{5} \right], \quad (7)$$

where ϕ_0 is the planet’s position angle and h_p is the pressure scale height at the planet’s orbital radius. This equation was derived from Rafikov (2002) Equation 44 using a power law index for the sound speed $\nu = -1/4$, as in Equation 2. In the linear regime, the perturbation is a one-armed spiral propagating from the planet both inward and outward and characterized by an opening angle depending only on the gas sound speed. The density perturbation’s maximum amplitude $\delta\Sigma/\Sigma_0 \simeq M_p/M_{th} \ll 1$, where Σ_0 is the unperturbed surface density profile.

If $M_p \geq M_{th}$, the density perturbations induced by the planet must be calculated by numerically solving the hydrodynamics equations. In this paper, we employ the publicly available code FARGO3D (Masset 2000, <http://fargo.in2p3.fr>) to simulate the disk’s interaction with planets having masses of 20, 100 and 1000 M_{\oplus} , corresponding to 1, 5 and 50 times the thermal mass respectively. Henceforth, we refer to these three hydrodynamical results as P20, P100, and P1000, respectively. We arbitrarily place the planets at 10 AU so that the perturbations on the disk structure have spatial scales observable with current infrared and millimeter-wave telescopes. The calculations are two-dimensional in the orbital plane, with the disk structure averaged over the perpendicular direction. The code setup is described in the appendix.

In Figure 1 are snapshots of the surface density in the P20, P100, and P1000 models after 300 orbits of the planet. To highlight the perturbations, we plot the ratio of the gas surface density

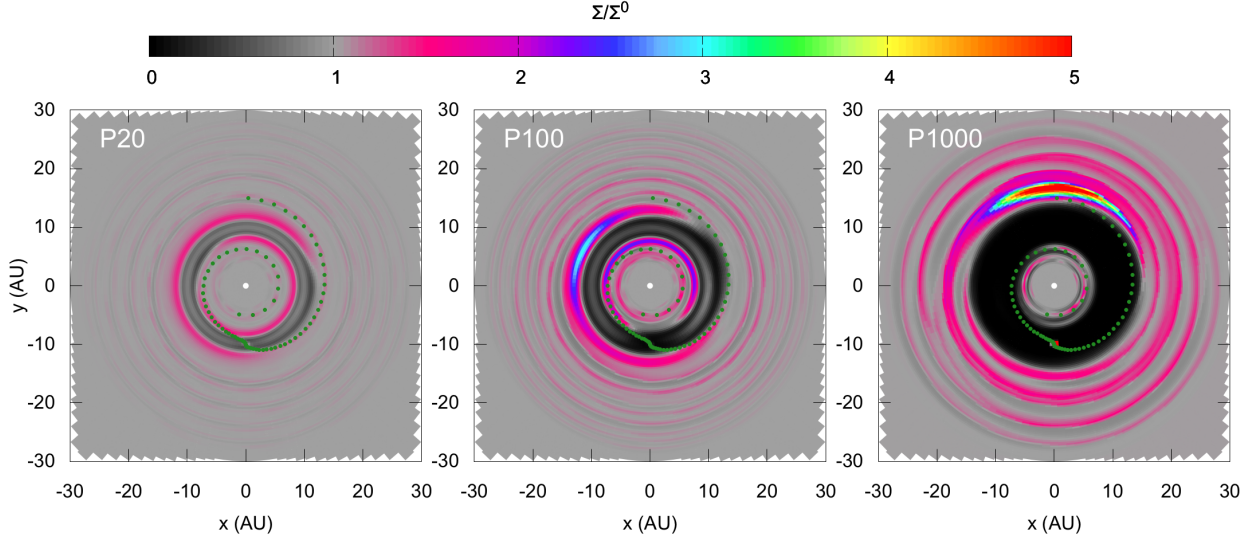


Fig. 1.— Surface density perturbations induced by planets of 20 (P20), 100 (P100) and 1000 (P1000) M_{\oplus} (left, center, and right panels, respectively) orbiting 10 AU from the star, after about 300 planet orbits ($\sim 10^4$ yr). The color scale shows the amplitude of the perturbations Σ/Σ^0 , relative to initial surface density profile Σ^0 defined by Equation 1. Green dots show the locus of the peak of the spiral density wave from the linear theory (Equation 7).

to that of the unperturbed disk defined by Equation 1. In the P20 model ($M_p = M_{th}$), the planet creates an $m = 1$ spiral wave, similar in shape and amplitude to the linear solution of Equation 7. Furthermore, the planet partially depletes a circular gap, reducing the surface density to about half its initial value over an annulus about 3 AU wide. Near the gap’s inner and outer edges are horseshoe structures in which the surface density varies by about 40% with azimuth.

More massive planets lead to stronger density perturbations. The gap is wider and more highly depleted, the spiral density wave has a higher amplitude and deviates more from the linear solution, and the azimuthal asymmetries grow. The non-axisymmetric structures take the form of anticyclonic vortices (Li et al. 2000). It is worth noting that while spiral density waves rotate at the planet’s Keplerian speed, the vortices formed at the gap edges rotate at the local orbital speed. This difference could profoundly impact the coupling between dust and gas, the disk thermal structure, and therefore the observability of such perturbations.

Finally, we point out that our hydrodynamic simulations’ outcomes depend on poorly known physical quantities such as the accretion stresses, as well as numerical parameters such as the smoothing length applied to the planet’s gravitational potential (see appendix). Investigating the interplay of these parameters is not the purpose of this paper. Instead, we use FARGO3D simply as a tool to produce surface density maps showing features similar to those observed in protostellar

disks, namely, circular gaps, azimuthal asymmetries, and spiral density waves.

2.3. Dynamical Coupling Between Dust and Gas

While the planet-disk interaction affects the distribution of circumstellar gas, the bulk of the disk’s opacity is carried by dust grains. The perturbations that planets induce on the disk temperature and continuum emission therefore depend on the relative distributions of dust and gas. The two are coupled by drag forces over the stopping time τ_s , which in the case of a Keplerian disk in hydrostatic equilibrium, can be written as

$$\tau_s \approx \frac{2\rho_i a}{\Sigma\Omega} \sim 1.1\text{yr} \times \left(\frac{a}{1\text{cm}}\right) \left(\frac{r}{10\text{AU}}\right)^{5/2} \quad (8)$$

(e.g., the review by Testi et al. 2014), where a is the particle size and ρ_i is the grains’ internal density. The right-hand form of the equation results from adopting a grain density of 2 g cm^{-3} and the surface density profile in Equation 1. The stopping time increases linearly with the grain size, so small particles are more closely coupled to the gas than big ones. To quantify the effect of planet perturbations on particles of different sizes, we compare the stopping time τ_s to the characteristic time scale for density perturbations τ_e calculated as follows. Spiral waves excited by a planet rotate at the Keplerian speed $\Omega_p = \sqrt{GM_\star/r_p^3}$. The relative angular speed between the spiral perturbation and a grain orbiting at a distance r from the star is therefore

$$\delta\Omega(r) = \Omega(r) - \Omega_p = \sqrt{GM_\star} \left(\frac{1}{r^{3/2}} - \frac{1}{r_p^{3/2}} \right). \quad (9)$$

If the density perturbation has a characteristic angular width $\delta\phi$, then during each orbit, a dust grain is entrained in the density wave only for the characteristic time

$$\tau_e \simeq \frac{\delta\phi}{\delta\Omega} = \frac{\delta\phi}{\sqrt{GM_\star}} \left| \frac{1}{r^{3/2}} - \frac{1}{r_p^{3/2}} \right|^{-1}. \quad (10)$$

Particles with $\tau_s \ll \tau_e$ will be distributed in the same way as the gas. If the gas surface density increases by $\delta\Sigma$, the dust surface density will simultaneously increase by the same proportion. Particles with $\tau_s \gg \tau_e$ on the other hand will not respond to the gas density variations. In between is the critical grain size a_{cr} , at which $\tau_s = \tau_e$. Particles smaller than a_{cr} trace the gas disturbances, while larger particle are free to respond to forces other than the gas drag. Using Equation 8 and 10, we write the critical grain size as

$$a_{cr}(r) = \delta\phi \times \frac{\Sigma(r)}{2\rho_i} \times \left| 1 - \left(\frac{r}{r_p}\right)^{3/2} \right|^{-1} \simeq 0.8\text{ cm} \times \left(\frac{10\text{AU}}{r}\right) \times \left| 1 - \left(\frac{r}{r_p}\right)^{3/2} \right|^{-1}, \quad (11)$$

where in writing the rightmost form, we assumed $\delta\phi = 10^\circ$. Figure 2 shows a_{cr} for $r_p = 10\text{ AU}$ and $\delta\phi = 5, 10$ and 15° . The critical grain size at 20 AU and 40 AU from the star ranges from 0.1 to 0.3

and 0.01 to 0.03 cm, respectively. This suggests that the grains dominating the cm- and mm-wave continuum emission will trace spiral density waves generated by a planet only close to the planet itself. Micron-sized particles, which are much smaller than the critical size, are well coupled to these perturbations throughout the disk.

The formation of gas-depleted gaps and vortices also affects the distribution of the dust relative to the gas. A gap’s outer edge is a local maximum in the gas pressure, and thus traps dust particles (Haghighipour & Boss 2003). Trapping is most efficient for particles with Stokes number $St = \tau_s \Omega \simeq 2\rho_i a / \Sigma$ close to unity. With the surface density profile in Equation 1, $St = 1$ corresponds to a grain size $a(St = 1) = 4.5 \text{ cm} \times (r/10\text{AU})^{-1}$. A gap’s outer edge will therefore preferentially trap cm- and mm-sized particles, while micron-sized dust remains coupled to the gas. Similarly, the gas pressure maxima at the centers of the vortices that develop on the gap’s outer edge preferentially concentrate large dust particles (Lyra et al. 2009; Birnstiel et al. 2013).

In summary, dust grains smaller than a few microns are likely to be well coupled to the gas through drag forces even in the presence of time-variable perturbations like those created by a planet. These small grains carry most of the opacity at optical and infrared wavelengths, and therefore control the starlight absorption and the disk’s temperature. However the continuum emission at mm and cm wavelengths comes from dust particles that are big enough to decouple from the gas. Thus, combining spatially-resolved observations of the gas and dust continuum emission at near-infrared and mm to cm wavelengths can potentially reveal both planet signatures and the dynamics of the larger particles.

2.4. Calculating Temperatures in Disks Perturbed by Planets

In this section, we describe the approach we adopt to compute the temperatures in disks perturbed by planets. We start by assuming that the disk beyond a few AU is heated only by the starlight. Accretion heating is neglected, which is a good approximation outside 1 AU for mass accretion rates less than about $10^{-8} \text{ M}_\odot \text{ yr}^{-1}$ (D’Alessio et al. 1998). We also assume that shock and compression heating related to the planet perturbations are negligible compared to the starlight heating. In this limit, the temperatures depend on the vertical distribution of dust particles smaller than a few μm , which dominate the opacity at optical and infrared wavelengths. Following the discussion of the previous section, we assume these particles are well coupled to the gas.

For smooth surface density profiles like that of Equation 1, the balance between gas pressure and stellar gravity leads to a hydrostatic equilibrium solution in which the disk’s top and bottom surfaces are concave, bending upward with increasing distance from the star. The temperature and the pressure scale height follow radial power-laws similar to Equations 2-5 (Chiang & Goldreich 1997; D’Alessio et al. 1998; Dullemond et al. 2001). By contrast, disks with non-monotonic surface density profiles like those resulting from disk-planet interactions have had their temperatures calculated only in a few cases. Turner et al. (2012) examined Jupiter’s effects on the Solar Neb-

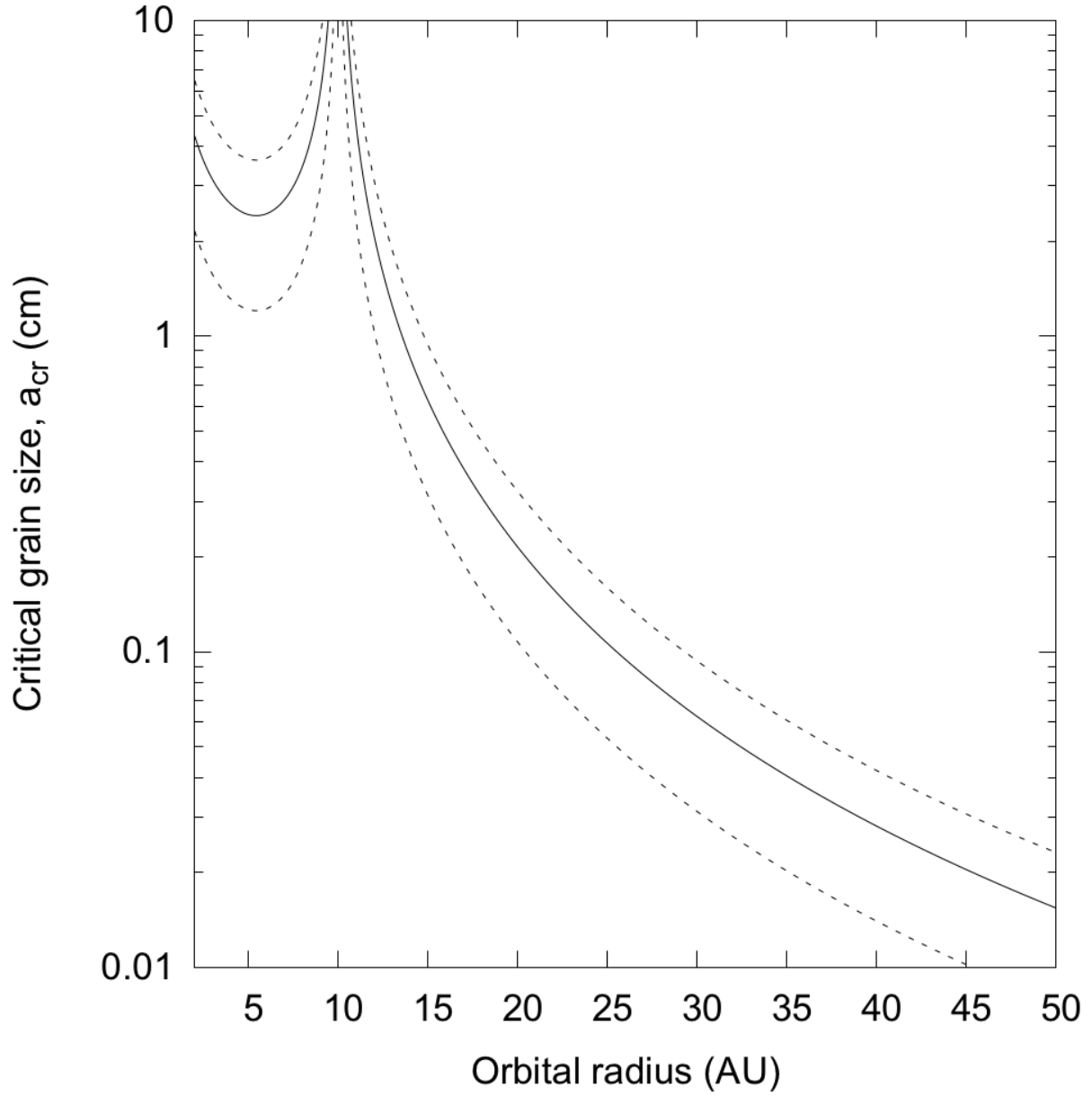


Fig. 2.— Critical dust particle size vs. distance from the star, for a planet orbiting at 10 AU. Only particles smaller than a_{cr} couple to spiral density perturbations raised by the planet. The solid line corresponds to an angular extent for the perturbation $\delta\phi = 10^\circ$, and the upper and lower dashed lines to $\delta\phi = 15^\circ$ and $\delta\phi = 5^\circ$, respectively.

ula, finding that the gap opened by the planet was up to twice as hot as the same location in an unperturbed Solar nebula. The low optical depth lets starlight scattered and reprocessed on the gap’s walls reach the midplane. Such planet-driven temperature perturbations could impact the

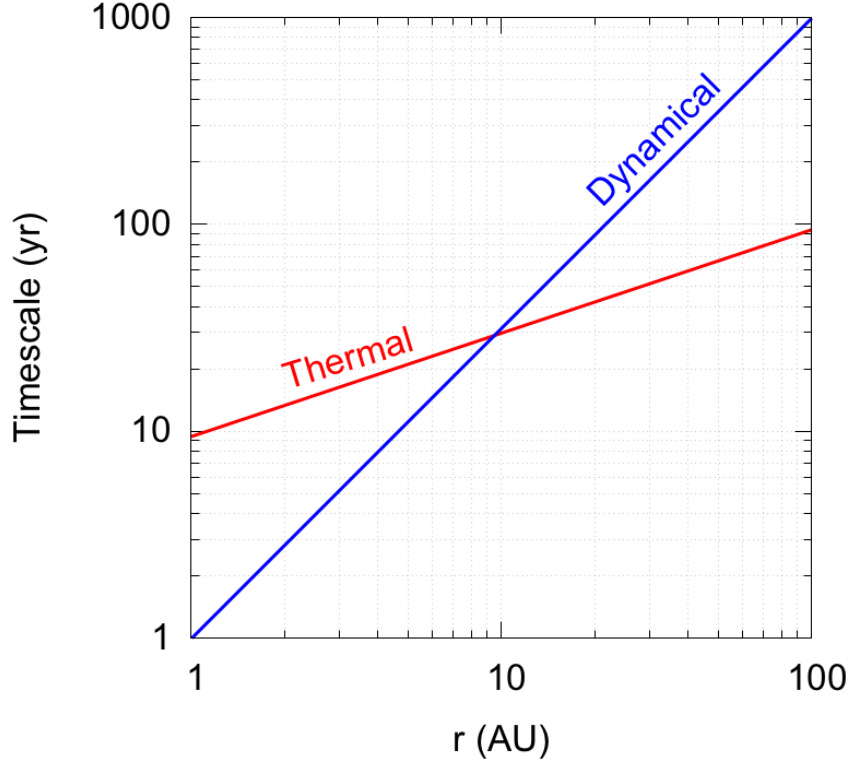


Fig. 3.— Thermal t_{th} and dynamical t_{dy} timescales vs. radius in the unperturbed disk model described in Section 2.1.

chemistry of the circumplanetary material, and perhaps the evolution of the disk itself.

Building on this result, we develop a numerical scheme to calculate the three-dimensional thermal structure of a disk perturbed by one or more planets. Our method is based on the consideration that the disk’s response to changes in illumination depends on the ratio of the thermal and dynamical time scales. The thermal time scale t_{th} is the time for the disk to heat or cool to a new thermal equilibrium, and the dynamical time scale t_{dy} is the time for the disk to reach hydrostatic equilibrium. Following Watanabe & Lin (2008), we write the thermal and dynamical time scales as

$$t_{th} = \frac{(\gamma + 1)}{2(\gamma - 1)} \frac{c_s^2 \Sigma}{\sigma T^4} \propto r^{1/2} \quad (12)$$

$$t_{dy} = \frac{2\pi}{\Omega} \propto r^{3/2} \quad (13)$$

Figure 3 shows the ratio of thermal to dynamical time for the unperturbed disk model described in Section 2.1. The two time scales assume the same value of about 29 yr at $r \simeq 9.5$ AU. We call these

the crossover time scale t_{cr} and radius r_{cr} , respectively. At $r \ll r_{cr}$, where $t_{dy} \ll t_{th}$, the disk can expand or contract in the vertical direction faster than its temperature can change. Thus after each change in the illumination, the disk will gradually approach thermal equilibrium while remaining close to hydrostatic equilibrium throughout. In the opposite extreme, at $r \gg r_{cr}$ where $t_{dy} \gg t_{th}$, the vertical structure varies slower than the temperature, so under changing illumination, the disk will quickly reach thermal equilibrium while spending some time out of hydrostatic equilibrium.

The following example illustrates these two time scales’ effects. Let’s assume, as in the P100 model, that a planet orbiting 10 AU from the star opens a gap, creating a local maximum in the gas and dust density near the gap’s inner edge (Figure 1). The higher dust density means more starlight is intercepted here, so the disk temperature begins increasing. Since the dynamics are quicker than the heating, the disk promptly expands to the hydrostatic equilibrium corresponding to the rising temperature. As the scale height increases, the gaps’ inner edge casts a taller shadow on the disk beyond. Under the decreased illumination, the outer regions quickly cool off. The shadowed parts contract toward the midplane on the local dynamical time scale, which is longer than the local thermal timescale, so even after the gap’s inner edge reaches thermal and hydrostatic equilibrium, the outer disk is still contracting towards the thinner state appropriate for its new temperature.

To track the disk’s response to the starlight across both regimes — with the thermal time scale the slower of the two, and with the dynamical time scale the limiting factor — we implement a sort of poor man’s radiation hydrodynamics. First, we bring the 2-D hydrodynamics calculation with the embedded planet to an approximate steady-state, and construct an initial guess at the 3-D density structure using the scale height $h^0(r)$ from the same radius in the unperturbed disk (Equation 5). Second, we send starlight into this structure using a Monte Carlo radiative transfer code, to determine a new distribution of temperature, sound speed, and hydrostatic equilibrium scale height, $\hat{h}^1 = c_s/\Omega$. Third, we account for the slower of the two timescales by restricting the change in the scale height to

$$\Delta h = \Delta \hat{h} \times \min \left(1, \frac{\Delta t}{\max(t_{dy}, t_{th})} \right), \quad (14)$$

where we set the timestep Δt equal to 10% of the initial crossover time t_{cr}^0 . At step n , this recipe is implemented as

$$h^n(r, \phi) - h^{n-1}(r, \phi) = [\hat{h}^n(r, \phi) - h^{n-1}(r, \phi)] \times \min \left\{ 1, \frac{0.1 t_{cr}^0}{\max[t_{dy}(r), t_{th}^{n-1}(r, \phi)]} \right\}. \quad (15)$$

Note that the scale height and thermal time depend on both the orbital radius r and azimuth ϕ . The second and third operations are then repeated, until from one timestep to the next, the temperature changes less than 5% on average. The procedure brings the model disk close to joint radiative and hydrostatic equilibrium by letting each patch expand or contract on its local timescale. This simplified dynamics lets us choose between the two alternative solutions in which the outer disk is (1) starlit, warm and flared, or (2) shadowed, cold and thin (Dullemond & Dominik 2004).

The radiative transfer calculations are made using the Monte Carlo code RADMC-3D, which follows the paths of large numbers of photons as they are absorbed and scattered by dust particles. Heating and cooling are calculated by adopting absorption and scattering opacities for spherical grains made of a mixture of astronomical silicates and carbonaceous materials, with relative abundances as in Pollack et al. (1994). The materials’ optical properties are mixed together using the Bruggeman theory to calculate the opacities for grains of a single size, which are then averaged over the size distribution $n(a) \propto a^{-3.5}$, with a ranging from 0.01 to 1000 μm . Anisotropic scattering is treated using the Henyey-Greenstein phase function. The absorption and scattering opacities, and asymmetry parameter g , are calculated using the Mie theory and are shown in Figure 4. We have varied the dust composition and grain size limits, with little effect on the disk’s final temperature structure.

Compared with Bitsch & Kley (2011) and Flock et al. (2013), we thus treat the gas flows in a highly simplified fashion, while giving the radiation field and temperature the comprehensive Monte Carlo transfer treatment. The method yields three kinds of model disks which we examine below: (1) in radiative equilibrium with the starlight, and in vertical hydrostatic balance, but unperturbed and planet-free, (2) disturbed by an embedded planet, and placed in radiative equilibrium with the starlight, but having the same scale heights $h^0(r)$ as the unperturbed model, so that it is hydrostatically out of balance, and (3) with the embedded planet, and placed in joint radiative and hydrostatic equilibrium using the poor man’s radiation hydrodynamics approach. We refer to these as models RH, P20R, and P20RH, respectively, when the planet has 20 M_\oplus . Thus our complete procedure yields a total of seven models: RH, P20R, P20RH, P100R, P100RH, P1000R, and P1000RH.

3. Results

3.1. Planet Perturbations’ Effects on Disk Temperatures

Figure 5 shows the midplane temperature distributions in the P20, P100 and P1000 models. The top row has the radiative equilibrium models, where we neglect the planets’ effects on the pressure scale height (cases P20R, P100R and P1000R). The bottom row has the models in both radiative and hydrostatic balance (P20RH, P100RH and P1000RH). To highlight the perturbations, we plot the ratio of perturbed to unperturbed temperature, the latter being as in Equation 2. Figure 6 shows the azimuthally averaged profiles of the temperature and surface density, ratioed with the unperturbed models.

The biggest disturbance in the temperature comes from the annular gap in the disk. Stronger temperature excursions generally go with stronger density perturbations, that is, with more massive planets. Among the $h = h^0$ cases, the temperature departs about $\pm 10\%$ in the P20R model, and up to $\pm 40\%$ in the P1000R model. The gap is cooler by about 10% and 20% in the P20R and P100R models, respectively, while temperatures near the gap edges increase by similar fractions.

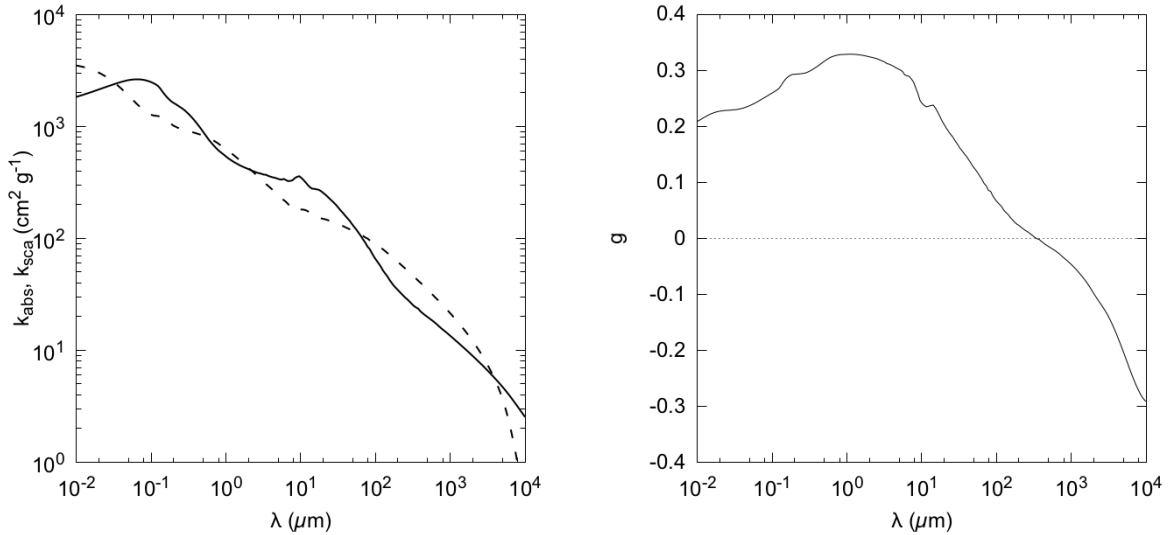


Fig. 4.— Left: Wavelength-dependent absorption (solid) and scattering (dashed) opacities adopted in calculating the disk’s temperature and appearance. Right: Wavelength-dependent scattering asymmetry parameter g .

In the P1000R model, temperatures both inside the gap and at its outer edge increase around 30%, while the gap’s inner edge cools by about 15%.

The disks that are also in hydrostatic equilibrium have significantly larger temperature excursions. What’s more, the temperature gradients across the gap are inverted, such that the inner edge is colder than the outer edge. In particular, the temperatures at the gap’s inner and outer edges are 36 and 37 K in P20RH, 34 and 41 K in P100RH, and 41 and 47 K in P1000RH, respectively. In the P20RH and P100RH models, the midplane within the gap is about 20% colder than in the unperturbed case, while it is almost 50% hotter in the P1000RH model. This difference is due to the fact that the gaps in the P20RH and P100RH models are optically thick to the starlight, while the gap is optically thin in the P1000RH model, allowing more scattered starlight and thermal re-emission to reach the midplane. The temperature variations in the P1000RH model are consistent with the results presented in Turner et al. (2012).

The outer edge of the gap opened by the planet is hotter in the radiative-hydrostatic equilibrium models P20RH, P100RH and P1000RH than in the corresponding $h = h^0$ cases, and hotter than the same location in the unperturbed model. The higher temperatures mean the gap outer edges puff up and cast shadows, cooling the disk beyond. In the P20RH and P100RH models, the shadows extend to 20 and 30 AU, respectively, where the decrease in stellar gravity with distance allows the disk thickness to increase to the point where the upper layers are once again in starlight. In the P1000RH model, the shadow extends beyond 50 AU where our model ends. The shadowed

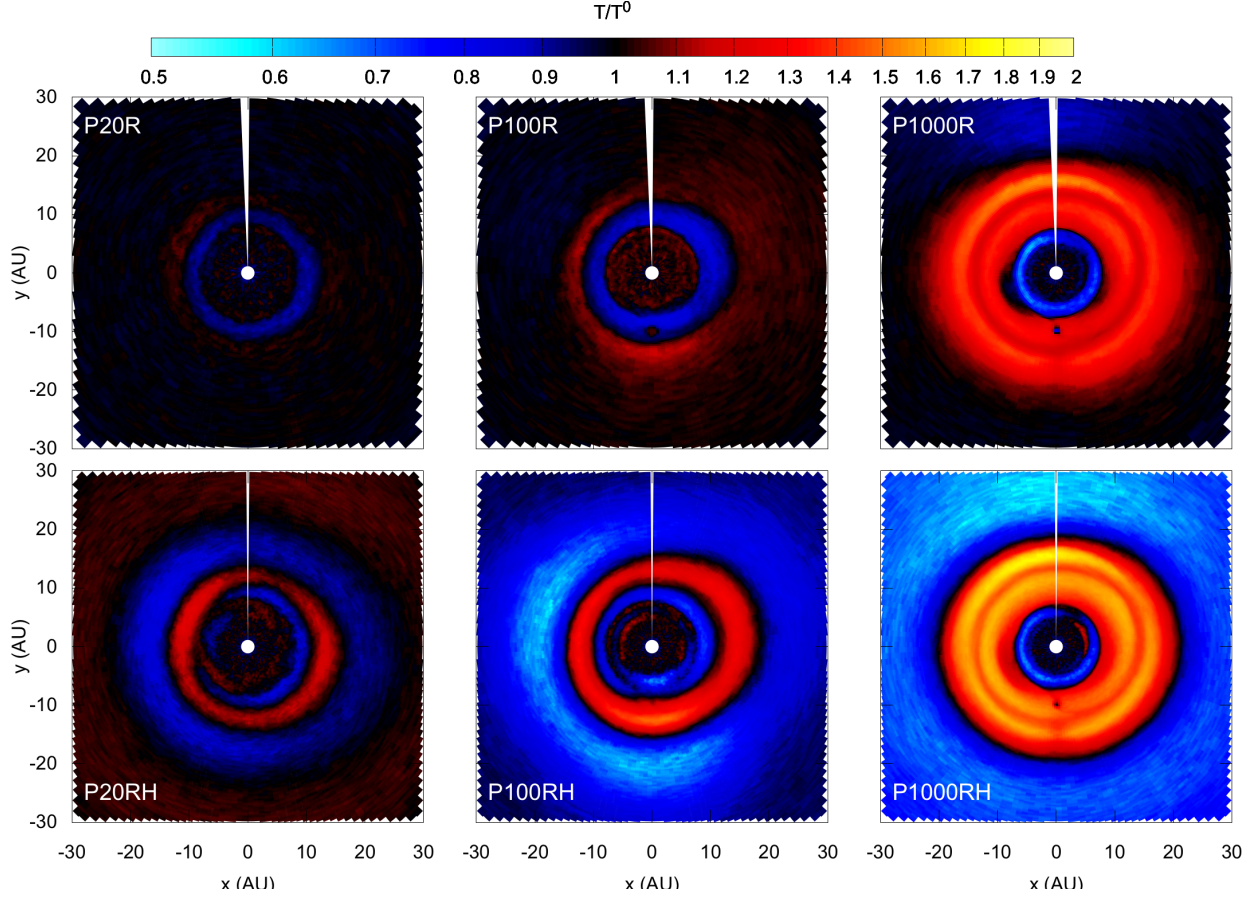


Fig. 5.— Midplane temperature perturbations in the models with planets of 20 (left), 100 (center), and 1000 M_{\oplus} (right). The top row shows models P20R, P100R and P1000R with the pressure scale height unchanged from the planet-free disk. The bottom row shows models P20RH, P100RH and P1000RH with pressure scale heights found by placing the disk in hydrostatic as well as radiative equilibrium.

regions’ weaker stellar illumination means temperatures are only about 70% of the unperturbed values, reducing the bolometric cooling rates roughly fourfold.

Finally, the temperature variations are slightly asymmetric, correlating to first approximation with the asymmetries in the surface density. For example, in the P1000RH model, the outer edge of the gap opened by the planet is hotter near the position of the density enhancement located at about 12 o’clock in figure 5 lower right panel. Along this same direction we register steeper temperature gradients between the hot gap edge and the cold outer shadowed region.

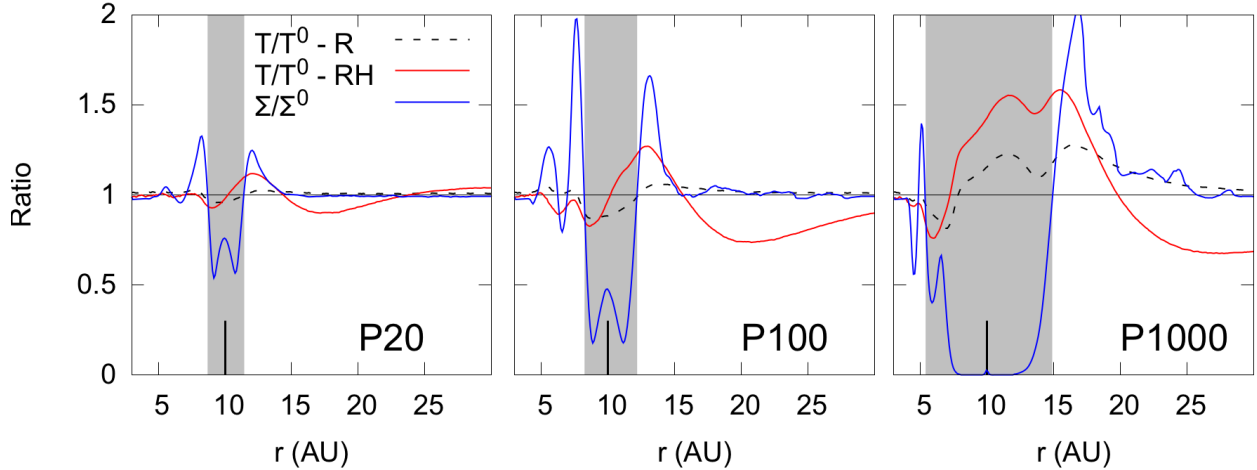


Fig. 6.— Azimuthally-averaged surface density and midplane temperature profiles in the 20-, 100-, and 1000- M_{\oplus} cases (left to right), divided by the planet-free model RH profiles. Dashed lines show models P20R, P100R and P1000R with the unperturbed scale heights, and solid lines are models P20RH, P100RH and P1000RH in hydrostatic as well as radiative equilibrium. Gray shading marks the gap opened by the planet, where surface densities are less than in the planet-free case.

3.2. Planet Perturbations’ Effects on Panchromatic Disk Continuum Emission

We construct synthetic images of all seven models using the ray-tracing module of RADMC3D, at wavelengths of $1\ \mu\text{m}$, $1\ \text{mm}$, and $1\ \text{cm}$. Whereas the near-infrared is dominated by stellar radiation scattered by sub-micron grains located in the disk’s surface layers, the emission at millimeter and centimeter wavelengths is mostly thermal, and originates from larger particles near the midplane. For simplicity, we generate synthetic images with the disk face-on. Furthermore, to better show the planet’s effects on the disk’s appearance, in all following figures we ratio each image with that of the unperturbed model RH.

The $1\ \mu\text{m}$ synthetic images appear in Figure 7. Their strongest features are dark and bright rings tracing, respectively, the gap opened by the planet and its outer edge. The hydrostatic equilibrium models also have a strong, broad dark ring where the gap’s puffed-up outer edge throws its shadow. The intensity of the bright ring at the gap’s outer edge depends sensitively on the disk’s vertical structure: its surface brightness is 2-5 times the planet-free case in the three R models which are out of hydrostatic balance, and 4-14 times the planet-free case in the three RH models, where hydrostatic balance is restored. In this and other ways, the R- and RH-models appear quite different, despite having identical surface density maps.

In the hydrostatic models, the region shadowed by the gap’s outer edge scatters starlight with surface brightness just a fraction of the same locations in the unperturbed disk. In contrast, the $h = h^0$ R-models show no such shadowing. Because of its sensitivity to the scale height, the scattered light is a poor tracer of the surface density. Relating scattered light features directly to

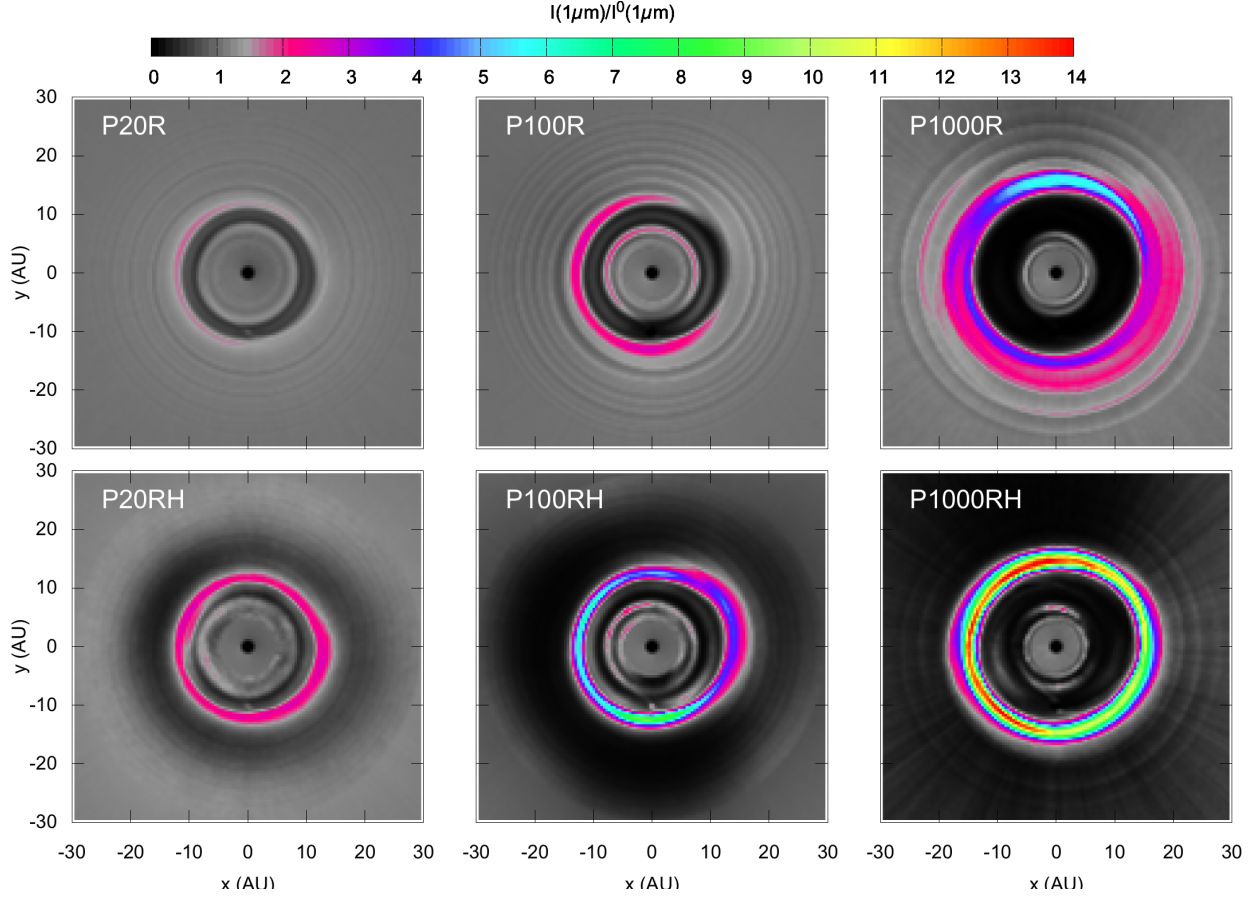


Fig. 7.— Maps of the 1 μm scattered light for the 20 (left), 100 (middle), and 1000- M_{\oplus} cases (right) viewed face-on. The top row shows the models in radiative but not hydrostatic equilibrium, P20R, P100R and P1000R. The bottom row has the corresponding models in both radiative and hydrostatic balance, P20RH, P100RH and P1000RH.

density variations can lead to serious errors.

Another notable feature of the scattered light images is that the planets' outer spiral density waves are obvious in the radiative equilibrium R-models, but largely hidden in the shadows in the radiative-hydrostatic equilibrium RH-models. For example, in the P1000R model, the spiral arms near 20 AU are 1.5 to 2 times brighter than surrounding regions, a contrast similar to the amplitude of the spiral density wave. However in the corresponding hydrostatic P1000RH model, the spiral arms disappear in the dark ring beyond the gap's outer edge. We will come back to this point in Section 5 in comparing models to observations.

Figures 8 and 9 show the ratio between the dust emission of the perturbed and unperturbed disk models at wavelengths 1 mm and 1 cm, respectively. As in the scattered light, the gaps opened

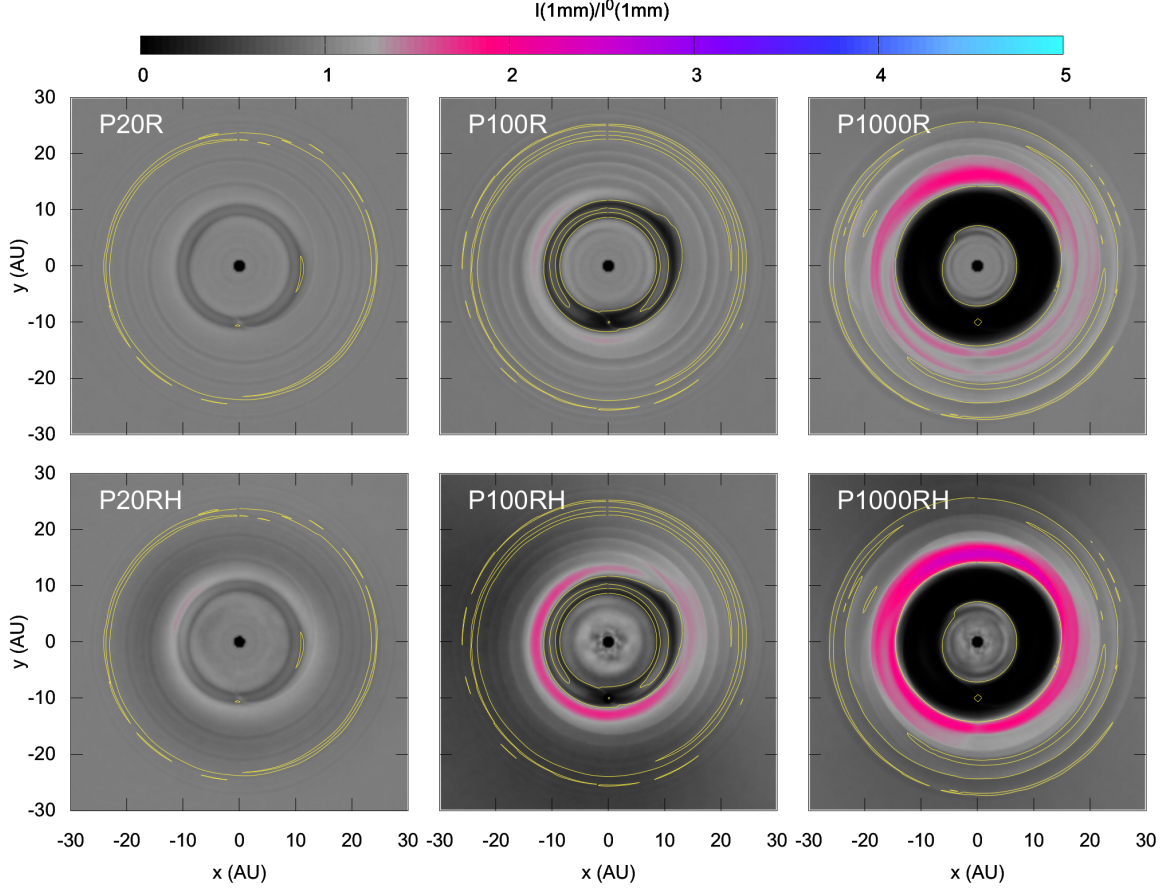


Fig. 8.— Maps of the 1 mm continuum emission from cases with planets of 20 (left), 100 (middle), and 1000 M_{\oplus} (right) viewed face-on. The top row shows the radiative equilibrium models P20R, P100R and P1000R. The bottom row has the radiative-hydrostatic models P20RH, P100RH and P1000RH. Yellow contours mark monochromatic optical depth unity.

by the planets appear as dark annuli, and the gaps’ outer rims appear as bright annuli. Azimuthal asymmetries due to vortices orbiting near the gaps’ outer edges are also visible.

For our assumed dust opacity and initial surface density, the 1 mm emission arising within 20 AU of the central star is mostly optically thick, and for this reason probes spatial variations of the temperature rather than the surface density. For example, in the P20RH model, the dark ring at the partially depleted, but still optically thick, gap comes from the low temperature in the gap discussed in Section 3.1 and is not due to the lower surface density. The large optical depth also reduces the visibility of the azimuthal asymmetries in the P100RH and P1000RH models. For example, in this last case the intensity ratio at the center of the vortex on the gap’s outer edge is 2.5, which is only about half the surface density ratio (Figure 1).

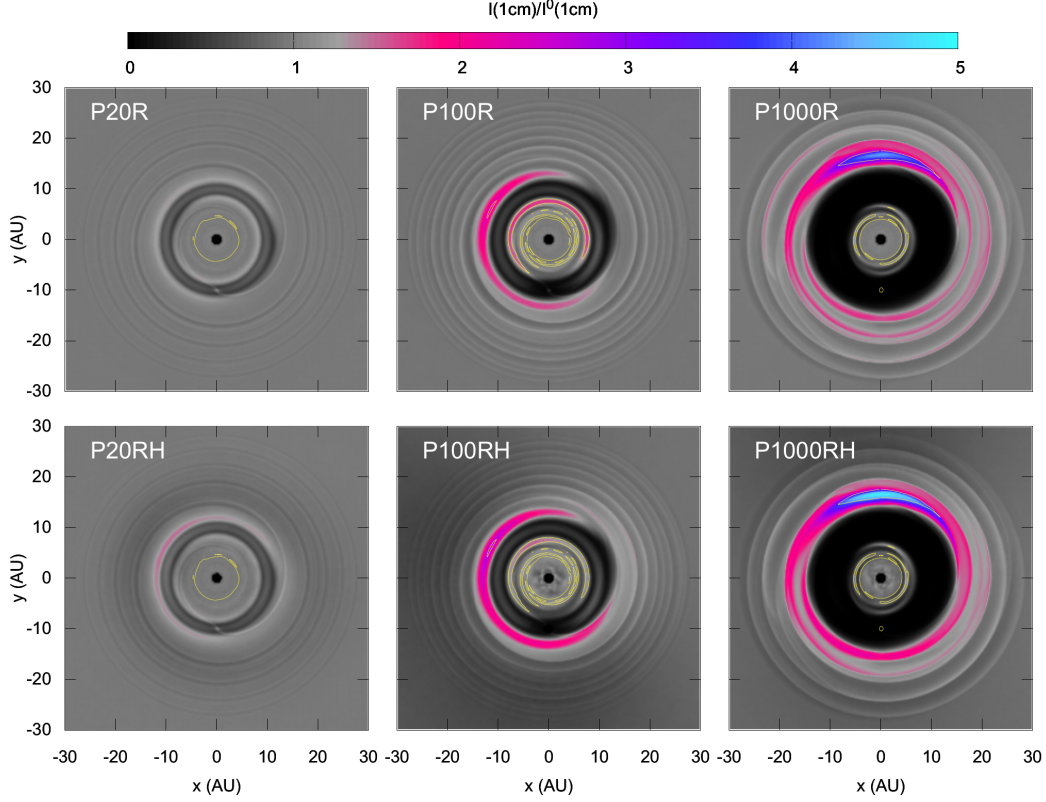


Fig. 9.— As Figure 8 but for the wavelength of 1 cm.

Since the 1 mm emission probes temperatures, it indirectly informs us about the vertical structure of the disk. In particular, the radiative-hydrostatic equilibrium RH-models have brighter gap outer edges, and fainter shadowed regions, than the radiative-equilibrium-only R-models. The starlight illumination is thus important for interpreting millimeter-wave observations of the optically-thick parts of protostellar disks.

The dust thermal emission at the wavelength of 1 cm from regions more than 5 AU from the star is mostly optically thin. It more closely probes the surface density perturbations caused by the planets. For example, at the gap’s outer edge the intensity varies with azimuth by factors of about 1.3 in the P20RH model, and about 5 in the P1000RH model, similar to the azimuthal ranges in the surface density shown in Figure 1. As with the 1 mm emission, the radiative equilibrium and radiative-hydrostatic equilibrium models look different at 1 cm wavelength, despite having the same surface density map, because their temperatures differ.

4. Consequences for Gas and Planet Dynamics

The main goal of our investigation is to understand young planets’ effects on the multi-wavelength dust continuum emission from protostellar disks, especially at the locations outside 5 AU where starlight dominates the heating. In pursuing this, we have found that the planet-disk interaction produces more than the long-predicted surface density perturbations: it also significantly perturbs temperatures across the disk. In this section, we elaborate on the temperature perturbations’ consequences for the dynamics of gas, dust and planets.

4.1. Heating and Cooling

We showed in Section 3.1 that perturbing planets of more than about $20 M_{\oplus}$ yield variations in the disk temperature with respect to a planet-free disk. This means that evolving the disk with an isothermal equation of state produces errors, and that reliable hydrodynamical modeling requires treating the heating and cooling. The need for something beyond a simple power-law relationship between temperature and density is illustrated in Figure 10, a map of the index $\gamma - 1$ in the relationship $T(r, \phi) \propto \rho^{\gamma-1}(r, \phi)$ applied to the disk’s evolution from the unperturbed state to the planet perturbation in radiative-hydrostatic equilibrium. The index is calculated by

$$\gamma - 1 = \log(T_m^{RH}/T_m^0)/\log(\rho_m^{RH}/\rho_m^0), \quad (16)$$

where T_m^0 is the midplane temperature of the unperturbed disk and T_m^{RH} is the midplane temperature in the RH-model. Isothermal evolution corresponds to $\gamma - 1 = 0$, and adiabatic evolution of molecular hydrogen corresponds to $\gamma - 1 = 0.4$. Clearly the evolution from the unperturbed to planet-perturbed models is not well described by a single value of γ . Note that $\gamma - 1$ is near zero within the gap opened by the planet not because the temperature is time-constant, but because the change in density is so much greater than the change in temperature. Generally, $\gamma - 1$ ranges from positive to negative values as we move from patches of the disk directly lit by the star to those lying in the shadows.

Another consequence of the changes in surface density and temperature across the disk is new values for the thermal time scale discussed in section 2.4. In figure 11 we show the ratio of the thermal to the dynamical time scale in the three radiative-hydrostatic equilibrium cases. The $20\text{-}M_{\oplus}$ model is broadly similar to the unperturbed profile in figure 3. The $100\text{-}M_{\oplus}$ model cools faster in the gap owing to the lower surface density, and cools slower in the outer shadowed region owing to the low temperatures. The $1000\text{-}M_{\oplus}$ model is a more extreme version of the $100\text{-}M_{\oplus}$ case, with shadows so deep and cold that temperatures change only over time scales comparable to or longer than the local orbital period. Apparently gap-opening planets can drastically change the surrounding disk’s thermal timescale, and thus its response to changing illumination.

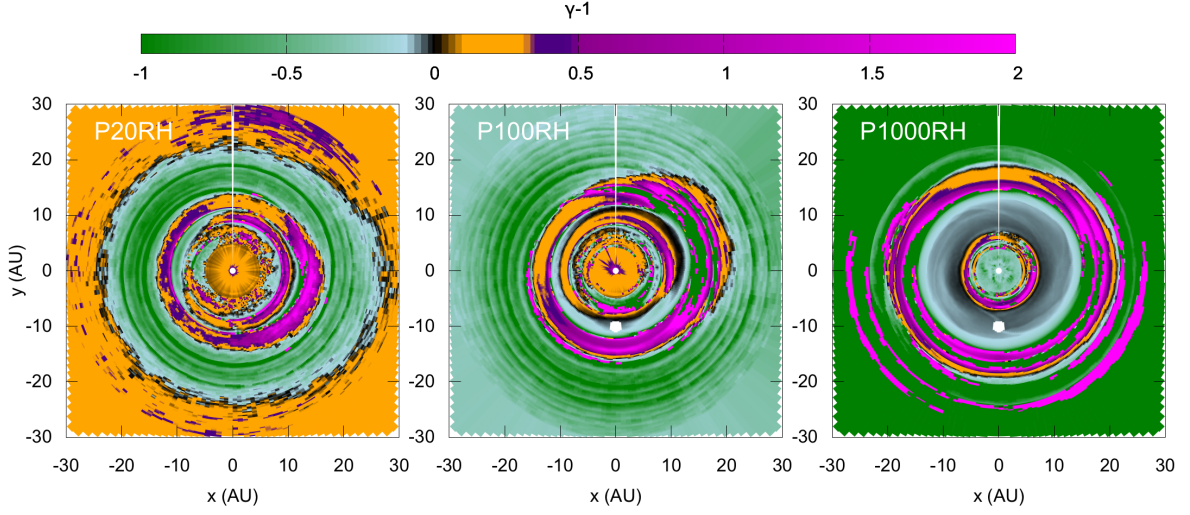


Fig. 10.— Maps of the power-law index in $T \propto \rho^{\gamma-1}$ describing the pointwise change in midplane temperature and density between the disk’s unperturbed state and its radiative-hydrostatic equilibrium with an embedded planet. The three panels show models P20RH, P100RH and P1000RH (left to right).

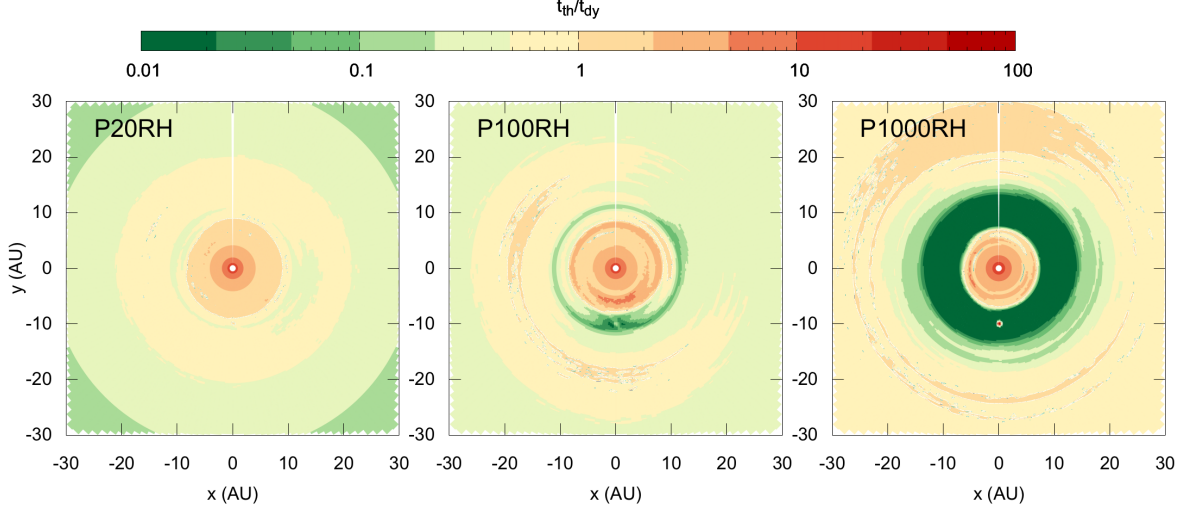


Fig. 11.— Ratio between the thermal and dynamical time scales. The three radiative-hydrostatic equilibrium models P20RH, P100RH and P1000RH appear from left to right.

4.2. Orbital Migration

Temperature perturbations caused by the planet-disk interaction might also affect the planet’s long-term orbital migration, which is governed by the gravitational forces exchanging angular mo-

mentum between planet and disk. If $M_p \ll M_{th}$, the rate and direction of migration are sensitive to the disk’s temperature and density structure. In a power-law model disk defined by $T \propto r^{-\beta}$ and $\Sigma \propto r^{-s}$, with β between 0.1 and 0.5, and s between 1 and 1.5, an Earth-mass planet migrates inward at a rate as high as 10^{-5} AU/yr (Ward 1997; Papaloizou & Terquem 2006). However, sufficiently steep radial temperature gradients can slow and even reverse the motion. In particular, outward migration is expected within a few AU of the star, where accretion is the main source of heating, while inward migration should occur at larger radii (Paardekooper & Mellema 2006; Lyra et al. 2010; Paardekooper et al. 2011; Bitsch & Kley 2011). Our results suggest that planets less than M_{th} perturb the temperatures too little to affect the migration rate. However, low-mass planets could find themselves migrating along the temperature gradients arising from a more massive companion’s interaction with their shared host disk.

Temperature perturbations’ effects on planets with $M_p \sim M_{th}$ have received too little attention. Jang-Condell & Sasselov (2005) found that the density and temperature perturbations near Neptune-mass planets can substantially slow their inward migration. Similar results were found by D’Angelo et al. (2003), who moreover argued that the lack of an appropriate energy equation is the main limitation in modeling such planets’ dynamics. Our results show that planets with close to the thermal mass (as in the P20 models) produce disturbances of about $\pm 20\%$ in the gas temperature (Figure 6). More importantly, in the P20RH model, the temperature gradient within the planet’s partially depleted gap turns positive. Quantifying the effects such perturbations have on the migration requires numerically integrating the torque exerted by the disk on the planet, which is beyond the scope of this work. Instead, we seek a qualitative understanding of the effects on low-mass planets’ migration by assuming the total torque Γ_{tot} is the sum of the Lindblad torque Γ_L and the horseshoe corotation torque Γ_{hs} expressed as (Paardekooper et al. 2011; Bitsch et al. 2013; Baruteau et al. 2014)

$$\Gamma_{tot} = \Gamma_L + \Gamma_{hs}, \quad (17)$$

$$\gamma \frac{\Gamma_L}{\Gamma_0} = -2.5 - 1.7\beta + 0.1s, \quad (18)$$

$$\gamma \frac{\Gamma_{hs}}{\Gamma_0} = \frac{7.9}{\gamma}(\beta - (\gamma - 1.0))s, \quad (19)$$

$$\Gamma_0 = \left(\frac{q}{h}\right)^2 \Sigma_p r_p^4 \Omega_p^2, \quad (20)$$

where γ is the ratio of specific heats ($\gamma = 1.4$ for molecular hydrogen gas). These equations imply that the total torque in the unperturbed model ($s = 1$, $\beta = 0.5$) is negative with $\Gamma_{tot}/\Gamma_0 = -1.9$, indicating inward migration as expected. In model P20RH, the surface density near the planet’s orbit also varies as r^{-1} , while the temperature scales as $r^{0.3}$ between 9 and 11 AU, an annulus that spans both the horseshoe region and the Lindblad resonances’ pileups inside and outside the planet’s orbit, and thus most strongly affects the planet. The positive temperature slope yields a more negative torque $\Gamma_{tot}/\Gamma_0 = -4.2$, indicating faster inward migration.

Finally, planets much more massive than M_{th} clear gaps, and so are thought to migrate fol-

lowing the global inflow of the circumstellar gas. The massive planets through their temperature perturbations might not affect their own migration rate, but they can alter the migration of nearby low-mass planets. For example, the P1000RH model in figure 5 at 15-20 AU, in the shadow of the gap’s outer edge, has midplane temperature scaling as $T \propto r^{-2.2}$. Across the same annulus, the surface density varies as $\Sigma \propto r^{-3.9}$. Equations 17-19 above indicate that a low-mass planet ($M_p \ll M_{th}$) orbiting here feels a positive torque ($\Gamma_{tot}/\Gamma_0 \sim 24$) so migrates rapidly outward. Positive torques also occur in the shadowed regions of the P20RH and P100RH models. Further out in each shadow, the temperature and surface density gradients flatten, and the torque turns negative. Migrating low-mass planets thus likely converge within the shadows cast by the gaps opened by massive planets.

5. Consequences For Interpreting Features in Protostellar Disks

5.1. Taxonomy

This section is devoted to the models’ implications for interpreting recent observations. Many protostellar disks feature annuli, crescents, and circular and spiral arcs in the dust and gas emission, as revealed through the improved sub-arcsecond mapping capabilities of infrared cameras such as HiCIAO/Subaru, Sphere/VLT, GPI/Gemini, and millimeter and centimeter arrays including CARMA, SMA, ALMA and the VLA. A list of such disks around stars not known to be double or multiple is in Table 1. Whether these structures, and their diversity, result from the interaction between the circumstellar material and forming planets, or are caused by other processes, is debated.

The SAO 206462 and J1604 systems are good examples of the diverse morphologies observed in protostellar disks (Figure 12). At sub-millimeter wavelengths, both disks show partially depleted dust cavities tens of AU in diameter (Pérez et al. 2014a; Zhang et al. 2014). However while the dust continuum in the SAO 206462 disk traces a crescent, the J1604 disk appears almost axisymmetric. At near-infrared wavelengths, the SAO 206462 disk exhibits an $m = 2$ grand design spiral, while the J1604 disk appears as a circularly symmetric annulus.

The crescents observed in the microwave regime come with a large spread of amplitudes, defined as the difference between the maximum and minimum flux densities measured at the same orbital radius divided by the minimum intensity, $a = (F_{max}(r) - F_{min}(r))/F_{min}(r)$. IRS 48 has the most prominent crescent observed so far, with an amplitude greater than 100; MWC 758, SAO 206462, LkHa 330 and SR 21 have much more moderate amplitudes between 1.5 and 3. Recent data show that crescents at sub-millimeter wavelengths are accompanied in most cases by near-infrared spiral features. This is the case for AB Aur, MWC 758, and SAO 206462.

The observations collected so far reveal a second trend: the earlier the spectral type of the star, the more complex the morphology of its disk. For example, the disks around HD 100546 and AB Aur, which have spectral types of B9.5 and A0, respectively, show multiple spiral features in

the near-IR. The AB Aur disk has a complex morphology also at millimeter wavelengths, showing a crescent and spiral features in the molecular line emission (Tang et al. 2012a). The disks around MWC 758 and SAO 206462, with spectral types between A5 and F7, have $m = 1$ or $m = 2$ spiral structures. In contrast, the disks around late G, K and M stars are mostly characterized by azimuthally symmetric rings at both infrared and millimeter wavelengths.

Finally, we note that in classifying perturbed disks, we explicitly avoid making use of the morphology of the molecular line emission observed with ALMA. The main reason is that spatially-resolved maps of the molecular line emission are available only for a few of the disks listed in Table 1. The molecular line emission however provides valuable information on the nature of the structures observed in disks. For example, ALMA observations of SAO 206462 and MWC 758 show that the ^{13}CO and C^{18}O are distributed much more nearly axisymmetrically than the dust. This suggests the crescent observed in the millimeter-wave continuum could result from the decoupling of large dust grains from the gas.

5.2. Comparing Models With Observations

Annuli: The models discussed in Section 3.2 show that the disk-planet interaction can naturally lead to ring-like structures in both the infrared scattered light and millimeter-wave emission, similar to those observed toward dynamically-cold disks. For example, the annular emission observed toward J160421.7-213028 is very similar to the synthetic maps for the P1000 model shown in the bottom-right panels of Figure 7 and 8. In both the model and the observations, the scattered light emission is confined to a narrow ring, whereas dust is present on a much wider area (Zhang et al. 2014). In our model, the ring seen in scattered light is narrow because the observed scattered light arises from the puffed-up outer edge of the gap opened by the planet. If, instead, the disk vertical structure were unaffected by the planet, scattered light would come from a wider annulus as shown in the top-right panel of Figure 7. Clearly the vertical structure is a key factor in interpreting scattered light maps of protostellar disks.

The effect of the vertical structure on the scattered light emission can be understood by analogy with a mountain illuminated by the Sun at sunset, as seen by an observer flying over it. Only the part of the mountain facing west will be illuminated, while its east side and the surrounding valleys will be in the dark. The shape of the illuminated side will depend on the shadows cast by the terrain westward of the mountain, but, in general, the higher the mountain, the larger the fraction lit by the setting Sun. The outer edge of the gap opened by the planet is similar to such a mountain. Indeed, this region is hotter, and therefore more puffed-up, than the surrounding area because it is directly illuminated by the star (Section 3.1).

Crescents: The disk-planet interaction produces vortices near the outer rim of the gap opened by the planet. This could naturally lead to the crescents observed in the millimeter- and centimeter-wave dust continuum emission, if the vortices concentrate sub-millimeter and millimeter-sized particles

Table 1: Protostellar disks around stars not known to be double or multiple, which show small-scale morphological features. The list includes only the objects with high-quality imaging at either infrared or millimeter wavelengths. The objects are ordered by stellar spectral type.

| Name | Sp.T. | M_{\star} | IR | mm | ref. |
|------------------|-------|-------------|-------------------------|------------------------|---------------|
| HD 100546 | B9.5 | 2.4 | Spiral arcs, $m \geq 3$ | Ring | ¹ |
| AB Aur | A0 | 2.0 | Spiral arcs, $m \geq 5$ | Crescent, $a \sim 4$ | ² |
| IRS 48 | A0 | 2.0 | Spiral arcs, $m \geq 1$ | Crescent, $a > 100$ | ³ |
| HD 163296 | A1 | 2.3 | Ring | Multiple rings | ⁴ |
| MWC 758 | A5 | 2.0 | Spiral arcs, $m \geq 2$ | Crescent, $a \sim 3$ | ⁵ |
| HD 169142 | A5 | 2.0 | Ring | Ring | ⁶ |
| SAO 206462 | F4 | 1.7 | Spiral arcs, $m \geq 2$ | Crescent, $a \sim 3$ | ⁷ |
| LkH α 330 | G3 | 2.5 | Spiral arcs, $m \geq 1$ | Crescent, $a \sim 1.5$ | ⁸ |
| SR 21 | G3 | 2.5 | Centrally peaked | Crescent, $a \sim 3$ | ⁹ |
| UX Tau | G8 | 1.5 | Ring | Ring | ¹⁰ |
| J160421.7-213028 | K2 | 1.0 | Ring | Ring | ¹¹ |
| LkCa 15 | K3 | 1.0 | Ring | Ring | ¹² |
| PDS 70 | K5 | 0.8 | Ring | Crescent, $a \sim 1.5$ | ¹³ |
| TW Hya | K6 | 0.8 | Ring | Multiple rings | ¹⁴ |

¹Grady et al. (2001); Ardila et al. (2007); Quanz et al. (2013a); Walsh et al. (2014)

²Hashimoto et al. (2011); Tang et al. (2012b)

³van der Marel et al. (2015); Follette et al. (2015)

⁴Garufi et al. (2014); Isella et al. (2016)

⁵Benisty et al. (2015); Isella et al. (2010)

⁶Quanz et al. (2013b); Momose et al. (2015)

⁷Muto et al. (2012); Pérez et al. (2014a)

⁸Akiyama et al. (2016); Isella et al. (2013)

⁹Follette et al. (2013); Pérez et al. (2014b); van der Marel et al. (2015)

¹⁰Tanii et al. (2012)

¹¹Mayama et al. (2012a); Zhang et al. (2014)

¹²Isella et al. (2014); Thalmann et al. (2010); Isella et al. (2012); Andrews et al. (2011a); Thalmann et al. (2014)

¹³Hashimoto et al. (2012, 2013, 2015)

¹⁴Rapson et al. (2015); Andrews et al. (2016)

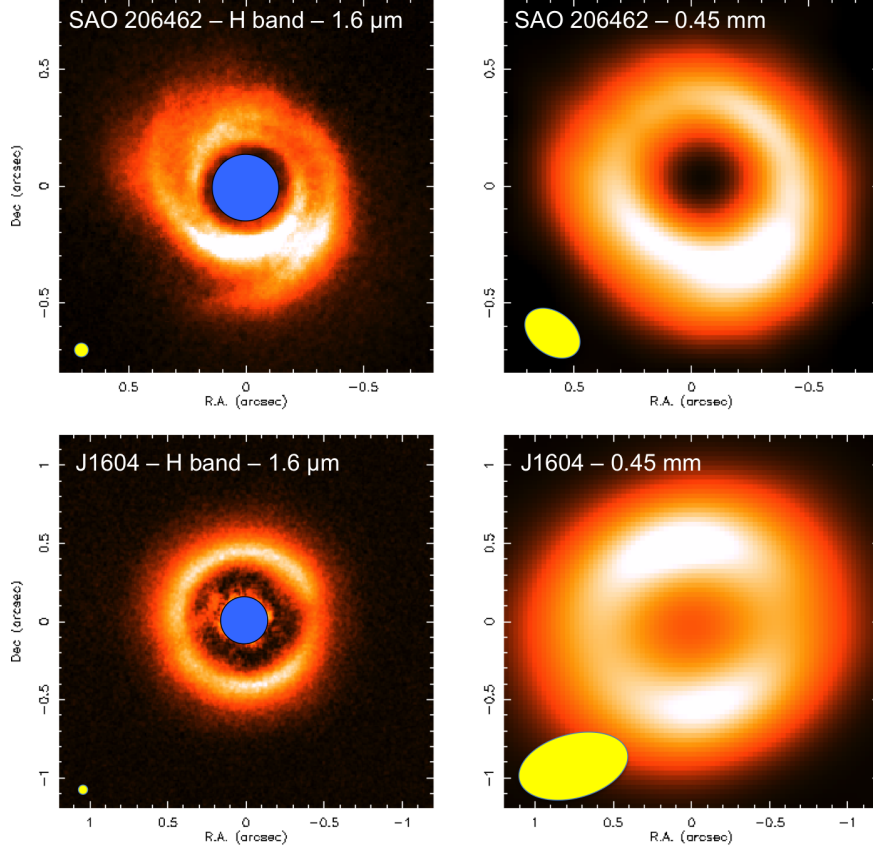


Fig. 12.— Maps of the SAO 206462 (top) and J1604 (bottom) disks recorded in the continuum emission at H-band (left) and 0.45 mm (right). These maps illustrate the variety of structures observed in protostellar disks, which include spiral and circular arcs, as well as crescents. The observations are taken from Muto et al. (2012), Pérez et al. (2014a), Zhang et al. (2014) and Mayama et al. (2012b).

through gas drag forces. The strongest concentrations toward gas pressure maxima are expected to occur for particles whose aerodynamic stopping time is comparable to the orbital period, so that the Stokes number $St \sim 1$ (Section 2.3).

The crescents observed in perturbed disks are characterized by azimuthal variations in the flux density with amplitudes between 1.5 and more than 100 (Table 1). Even if the dust emission is optically thin, and therefore traces the dust column density, measuring the amplitude of the crescent is by itself insufficient to determine the degree to which the dust has been concentrated relative to the gas. We must also measure the azimuthal variation in the gas density. Nevertheless, hydrodynamic models indicate that a single planet generates azimuthal perturbations on the gas

surface density of up to a factor of a few (Figure 1). Similar values are obtained with multiple planets (e.g. Isella et al. 2013). Therefore, the large-amplitude crescent observed IRS 48 (amplitude > 100) requires dust and gas be dynamically decoupled.

In principle, the degree of separation of dust and gas can be measured by comparing maps of the optically-thin dust and trace molecular species’ emission. The latter is the best probe of the total gas mass, since the main component, molecular hydrogen, is not itself observable. However, the conversion from other molecules’ line emission to the column density of H_2 is hampered by uncertainties in the molecular abundance, which depends on chemical reactions as well as the temperature (Willacy & Langer 2000; Aikawa et al. 2002; Qi et al. 2015). Quite surprisingly, none of the disks characterized by crescents in the dust continuum emission shows similar structures in the molecular gas. In fact, the dust and gas emission anti-correlate, suggesting that perhaps the concentration of dust triggers chemical reactions that destroy molecules or remove them from the gas phase, for example through freeze-out onto the grains (van der Plas et al. 2015; van der Marel et al. 2015).

Spirals: Interpreting protostellar disks with grand design spirals in the framework of planet-disk interaction is problematic. Our models suggest the planet-generated spiral density waves have quite weak signatures at near-infrared wavelengths (Figure 7). This is because the outer edge of the gap cleared by the planet casts a shadow on the outer disk, strongly reducing the visibility of any spiral feature located outside the gap. A similar result was obtained by Juhász et al. (2015), who constructed synthetic scattered light images for a disk perturbed by planets, assuming that the disk pressure scale height scales as a power law with the radius (their Figure 2). As shown in Figure 7, the spirals’ visibility at infrared wavelengths is even worse when the pressure scale heights are consistent with hydrostatic equilibrium.

Another problem is the large pitch angles of the spiral arms observed in the near-infrared. Since the pitch angle of a spiral density wave launched by a planet increases with the gas temperature (see Section 2.2), large angles imply high temperatures. By comparing MWC 758 observations with the analytical solution of Equation 7, Benisty et al. (2015) inferred that the disk temperature at the location of the spirals should be several hundred degrees Kelvin, at least ten times greater than the temperature calculated based on the stellar flux received. How can the disk reach such high temperatures? Lyra et al. (2016) suggest the disk might be heated as the density waves launched by a massive planet ($5 M_J$) shock the circumstellar gas. Note that this works only if the heat is not radiated away, but remains in the disk from one shock passage to the next – that is, t_{th} must exceed t_{dy} , which in our initial disk model happens only within 10 AU of the star.

Furthermore, the shock heating is deposited preferentially near the planet’s innermost Lindblad resonances, which lie close to the edges of the gap the planet opens in the disk (Figure 3 of Lyra et al. 2016). Hot gas at the Lindblad resonances would mean a taller outer edge for the gap, which could even reduce the visibility of spiral waves in the scattered light emission. It is also not yet clear whether such hot material would produce hot spots visible in the mid-infrared or

millimeter continuum emission. ALMA observations constrain the temperatures of dust and gas (most gas measurements are of carbon monoxide) near the spiral arms to less than 40 K (Isella et al. submitted; Muto et al. 2015).

As a solution to both the spirals’ visibility and the pitch angle problem, Dong et al. (2015b) have suggested the observed spiral waves might be excited by a massive planet ($> 5M_J$) orbiting outside the cavities observed at millimeter wavelengths, and beyond the spiral features observed in the near-infrared. In this model, the observed spirals correspond to the arms propagating inward from the planet orbital radius. This is similar to the picture proposed by Muto et al. (2012) to explain the large pitch angle of the spiral features observed in the SAO 206462 disk. In the case of MWC 758, Dong et al. (2015b) calculate that the planet would have an orbital radius of about 160 AU (their Figure 4). For this model to work, the planet must be very young. In particular, the age of the planet must be less than the time required to open a gap in the disk. This is because once the gap is fully opened, the part of the spiral density wave with the largest pitch angle will be located within the dust depleted gap, making the spiral disappear at infrared wavelengths. In the specific case of MWC 758, Dong et al. (2015b) manage to reproduce the observations by halting the hydrodynamic simulation after 20 orbits of the planet, or about 0.3×10^5 yr for an orbital radius of 160 AU. The entire gap opening phase takes 0.6×10^5 to 1.5×10^5 yr, depending on the accretion stress. If the observable lifetime of the spiral is so short, objects like MWC 758 and SAO 206462 should be a small fraction, probably less than 10%, of the disk population forming giant planets at large separation. This seems to conflict with the fact the spiral arcs are observed in the majority of perturbed disks around early type stars.

A third hypothesis, advanced by Dong et al. (2015a), is that the spirals observed in scattered light result from the disk’s gravitational instability. To be gravitationally unstable, disks must be massive. Dong et al. (2015a) find that the spiral structures in SAO 206462 and MWC 758 require disk masses of 0.25 and 0.5 M_\odot , respectively. These are much greater than the masses derived from observations of the millimeter-wave dust emission, which suggest instead masses of about 0.025 and 0.01 M_\odot , respectively (Isella et al. 2010; Andrews et al. 2011b).

Finally, a fourth hypothesis is that the spiral features are due to material orbiting near the star which casts shadows that appear as spirals because they sweep across the disk at the finite speed of light (Kama et al. 2016). Forming bright spiral arms this way requires notches in the screening material to let through narrow beams of starlight, while variability surveys suggest narrow-angle obscuration is more common (Cody et al. 2014; Stauffer et al. 2015).

Clues to the causes of the spiral features observed in the near-infrared might be gained by looking at the ensemble of perturbed disks listed in Table 1. For example, as noted above, five of the seven disks around A and F stars are characterized by spiral features, while no spirals are detected in the disks of the four G and K type stars for which observations exist. Whereas we cannot exclude that this trend might be an artifact of the small sample, the available observations suggest that the formation of spiral arms somehow depends on the stellar mass.

It is worth noting that early-type stars are mostly in binary or multiple systems. The multiplicity fraction of mature G-type stars is 57%, complete down to a companion-to-primary mass ratio of 0.1. This fraction is higher among A- and F-type stars. The large fraction of multiples among the main-sequence stars suggests a correspondingly high fraction of multiples among young early-type stars. Based on this consideration, we suggest that the observed perturbations might be due to the presence of yet unseen, close separation, stellar mass companions, instead of planets. A companion with greater mass will excite stronger density waves, which might warm up the circumstellar gas through shock heating, as remarked above, or induce other kinds of instability in the disk. The heating from the companions should also be taken into account in future hydrodynamical modeling of this scenario.

A companion might be responsible for at least one of the dynamically-hot disks. The star HD 142527 has a $0.13 M_{\odot}$ companion orbiting between 10-20 AU (Lacour et al. 2016). This binary system has a mass ratio of 15, much lower than those in the models we present here, which range from 330 to 16700. The dynamically-hot disks listed in Table 1 are not known to have stellar companion, but most of the observations obtained so far are insensitive to companions at separations less than 10 AU (e.g. Willson et al. 2016).

6. Conclusions

Protostellar disks show central cavities, bright and dark rings, and spiral arms that could be from gravitational perturbations by low-mass stellar or planetary companions, which are expected to be nearly ubiquitous. However, many of the features can also be made by processes intrinsic to the disks, with no companion bodies present. Few or no planets have yet been conclusively identified embedded in protostellar disks, and attempts to connect the observed spiral arms to planets on particular orbits appear to require either rather high disk temperatures, or that we have caught the planets in the short-lived stage when they are crossing the threshold mass for opening a gap. Non-planet mechanisms also have difficulties. Gravitational instability suffers from requiring disk masses much larger than measured, while light-travel-time effects make bright spirals only with specific patterns of obscuration by material near the star.

To address these issues we have explored how young planets alter protostellar disks’ emission at near-infrared, millimeter and centimeter wavelengths, using 2-D vertically-averaged hydrodynamical modeling to map the surface density around the planet, and 3-D radiative transfer calculations to obtain the vertical distribution of material and the temperature structure. We consider planets with masses just at the threshold for tidally clearing a gap around their orbit, and planets with masses five and fifty times greater, which open substantial gaps. We obtain model disks that are in radiative equilibrium with the starlight heating, and in vertical hydrostatic balance. The planets modify the disks’ structure and appearance as follows:

1. A planet massive enough to open even a partial gap in the disk lets additional scattered

starlight and re-emitted infrared radiation reach and warm the midplane.

2. The light scattered to our telescopes reveals the parts of the disk directly lit by the star. The starlight’s grazing angle of entry means that even small features on the disk surface cast long shadows. The planet-carved gap’s outer wall in particular receives extra starlight heating and puffs up, throwing a shadow across the disk beyond. The shadow appears in scattered light as an additional dark ring, which could be mistaken for a gap opened by another more distant planet.
3. The shadow is much darker and colder in models with the disk placed in vertical hydrostatic equilibrium, than in those where the scale heights are left unchanged from the disk without planets. Our hydrostatic model with 100- M_{\oplus} planet has a scattered light surface brightness contrast between gap outer wall and shadow that is almost an order of magnitude greater than the model where the scale heights are as in the planet-free disk.
4. For a disk mass and size rather typical of nearby protostellar disks, the millimeter emission arising from the regions where most planets are expected to form is optically thick, and therefore tells us about the dust temperature rather than the surface density. The same disk is mostly optically thin at centimeter wavelengths, which therefore trace perturbations in the dust surface density such as those induced by planets.
5. The shapes and contrast levels of the brightest areas in the synthetic millimeter and centimeter continuum images depend on whether we enforce hydrostatic equilibrium, even though this leaves surface densities unchanged, because the altered scale heights change the pattern of starlight illumination, causing shifts in temperature.

A common theme in these results is that when interpreting protostellar disk features as caused by an embedded planet, we cannot safely assume the temperature at each position is fixed, but must consider radiative heating and cooling. The planet disturbs the disk, changing where the starlight falls, which changes the temperatures, which further alters the shape of the disk’s surface. This cascade of effects impacts the architecture of the nascent planetary system: the temperature gradients in the shadows cast by the puffed-up outer rims of the gaps opened by our more massive planets are such that additional low-mass planets’ orbital migration will converge in the shadows.

The coupling of dynamics with radiative transfer which we have explored will help in understanding the concentric rings observed in some disks. However several aspects of the observations remain mysterious. In particular, we have no good explanation for the spiral features. In fact, we have turned up evidence that they are probably not caused by planets, since under hydrostatic equilibrium the outer rim of the planet-opened gap casts a shadow so deep, it largely hides the outer arm of the planet’s spiral wave. Also still unclear is why more-massive stars often show spiral arms, while low-mass stars’ disks typically have azimuthally symmetric rings.

Two limitations of the models presented here are worth mentioning. The first is connected with the millimeter and centimeter emission, which come from sub-millimeter to millimeter-sized dust

grains that are dynamically well-coupled only to dense gas near the planet (Section 2.3). Since these big grains’ interaction with the gas depends on their poorly-known aerodynamic properties and the distribution of turbulence, we have focused on the limit where the dust and gas are well-mixed, leaving treatment of the gas-dust dynamical interaction for future work. The second limitation is that the radiative and hydrostatic equilibrium approximations are valid only if the illumination is time-steady, which holds if the shadow-casting structures are axisymmetric. However some disturbances, such as a Rossby vortex on the outer rim of the gap opened by a massive planet, are clearly non-axisymmetric and cast time-varying shadows. The illumination may vary faster than the outer disk can respond, in which case some parts of the system will be perpetually out of hydrostatic balance, always shrinking or expanding towards the scale height consistent with their momentary temperature.

A. FARGO setup

The hydrodynamic calculations of the planet-disk interaction are performed using the GPU version of the FARGO3D code. Simulations are run in two dimensions using a polar grid consisting of 1500 cells in both the radial and azimuthal directions, for a total of 2.25×10^6 cells. The radial grid is linearly spaced and extends from 0.3 to 3 times the planet’s orbital radius. Each cell’s radial size is 0.02 AU. By comparison, the disk pressure scale height at the position of the planet is 0.43 AU (Equation 5), corresponding to 22 cells.

The disk feels the pull of the planet’s gravity, while the planet is fixed on its initial circular orbit at 10 AU. The planetary gravitational potential is smoothed by setting the *ThicknessSmoothing* parameter to 0.6. Following Kley et al. (2012), this value of the potential smoothing length provides the best agreement between two- and three-dimensional hydrodynamical calculations. The kinematic viscosity is set to zero across the entire disk. We run each calculation to about 300 orbits, by which time the surface density map is almost time-steady.

B. RADMC-3D setup

The disk temperature and emitted radiation are calculated using the Monte Carlo radiative transfer code RADMC-3D available at <http://www.ita.uni-heidelberg.de/~dullemond/software/radmc-3d>. We adopt spherical coordinates with 500 cells in the radial direction, 370 cells in the azimuthal direction, and 160 cells in the polar direction. The radial cells are equally spaced between 0.5 and 50 AU, corresponding to a radial extent of about 0.1 AU. The azimuthal grid extends from 0 to 2π radians, and the polar grid from 60 to 120° , where 0° is the disk’s rotational axis, and 90° is the midplane. We have performed several tests to make sure the transfer calculations’ results are unaffected by the number of cells and the extent of the polar grid.

Each Monte Carlo simulation involves 10^9 photon packets. Computing the radiative equilib-

rium temperature is by far the slowest part of a timestep in the poor man’s radiation hydrodynamics scheme, requiring about 1 hr of wall-clock time on a machine equipped with 20 Intel Xeon 2.80-GHz processors. The midplane, which is the optically thickest part of the disk, and so the least often visited by diffusing photon packets, is then well enough sampled to reduce the temperatures’ statistical noise below 5% everywhere.

A.I. and N.J.T. thank Mario Flock, Cornelis Dullemond, and Wladimir Lyra for helpful discussions, and acknowledge support from the NASA Origins of Solar Systems program through award NNX15AB06G and from the JPL Research & Technology Development Program through award R.16.183.037. This work was carried out in part at the Jet Propulsion Laboratory, California Institute of Technology, under a contract with NASA.

REFERENCES

- Aikawa, Y., van Zadelhoff, G. J., van Dishoeck, E. F., & Herbst, E. 2002, *A&A*, 386, 622
- Akiyama, E., et al. 2016, ArXiv e-prints
- Andrews, S. M., Rosenfeld, K. A., Wilner, D. J., & Bremer, M. 2011a, *ApJ*, 742, L5
- Andrews, S. M., & Williams, J. P. 2007, *ApJ*, 671, 1800
- Andrews, S. M., Wilner, D. J., Espaillat, C., Hughes, A. M., Dullemond, C. P., McClure, M. K., Qi, C., & Brown, J. M. 2011b, *ApJ*, 732, 42
- Andrews, S. M., et al. 2016, *ApJ*, 820, L40
- Ardila, D. R., Golimowski, D. A., Krist, J. E., Clampin, M., Ford, H. C., & Illingworth, G. D. 2007, *ApJ*, 665, 512
- Baruteau, C., et al. 2014, *Protostars and Planets VI*, 667
- Batalha, N. M., et al. 2013, *ApJS*, 204, 24
- Benisty, M., et al. 2015, *A&A*, 578, L6
- Birnstiel, T., Dullemond, C. P., & Pinilla, P. 2013, *A&A*, 550, L8
- Bitsch, B., Crida, A., Morbidelli, A., Kley, W., & Dobbs-Dixon, I. 2013, *A&A*, 549, A124
- Bitsch, B., & Kley, W. 2011, *A&A*, 536, A77
- Bryden, G., Chen, X., Lin, D. N. C., Nelson, R. P., & Papaloizou, J. C. B. 1999, *ApJ*, 514, 344
- Chiang, E. I., & Goldreich, P. 1997, *ApJ*, 490, 368

- Cody, A. M., et al. 2014, *AJ*, 147, 82
- D’Alessio, P., Canto, J., Calvet, N., & Lizano, S. 1998, *ApJ*, 500, 411
- D’Angelo, G., Henning, T., & Kley, W. 2003, *ApJ*, 599, 548
- Dong, R., Hall, C., Rice, K., & Chiang, E. 2015a, *ApJ*, 812, L32
- Dong, R., Rafikov, R. R., & Stone, J. M. 2011, *ApJ*, 741, 57
- Dong, R., Zhu, Z., Rafikov, R. R., & Stone, J. M. 2015b, *ApJ*, 809, L5
- Dong, R., Zhu, Z., & Whitney, B. 2015c, *ApJ*, 809, 93
- Dullemond, C. P., & Dominik, C. 2004, *A&A*, 417, 159
- Dullemond, C. P., Dominik, C., & Natta, A. 2001, *ApJ*, 560, 957
- Flock, M., Fromang, S., González, M., & Commerçon, B. 2013, *A&A*, 560, A43
- Follette, K. B., et al. 2013, *ApJ*, 767, 10
- . 2015, *ApJ*, 798, 132
- Garufi, A., Quanz, S. P., Schmid, H. M., Avenhaus, H., Buenzli, E., & Wolf, S. 2014, *A&A*, 568, A40
- Goldreich, P., & Tremaine, S. 1978, *ApJ*, 222, 850
- Goodman, J., & Rafikov, R. R. 2001, *ApJ*, 552, 793
- Grady, C. A., et al. 2001, *AJ*, 122, 3396
- Haghighipour, N., & Boss, A. P. 2003, *ApJ*, 583, 996
- Hashimoto, J., et al. 2011, *ApJ*, 729, L17
- . 2012, *ApJ*, 758, L19
- . 2013, *ApJ*, 775, L33
- . 2015, *ApJ*, 799, 43
- Hayes, J. C., & Norman, M. L. 2003, *ApJS*, 147, 197
- Isella, A., Carpenter, J. M., & Sargent, A. I. 2009, *ApJ*, 701, 260
- Isella, A., Chandler, C. J., Carpenter, J. M., Pérez, L. M., & Ricci, L. 2014, *ApJ*, 788, 129
- Isella, A., Natta, A., Wilner, D., Carpenter, J. M., & Testi, L. 2010, *ApJ*, 725, 1735

- Isella, A., Pérez, L. M., & Carpenter, J. M. 2012, *ApJ*, 747, 136
- Isella, A., Pérez, L. M., Carpenter, J. M., Ricci, L., Andrews, S., & Rosenfeld, K. 2013, *ApJ*, 775, 30
- Isella, A., et al. 2016, *Phys. Rev. Lett.* submitted, 0
- Jang-Condell, H. 2008, *ApJ*, 679, 797
- . 2009, *ApJ*, 700, 820
- Jang-Condell, H., & Sasselov, D. D. 2005, *ApJ*, 619, 1123
- Jang-Condell, H., & Turner, N. J. 2012, *ApJ*, 749, 153
- . 2013, *ApJ*, 772, 34
- Jin, S., Li, S., Isella, A., Li, H., & Ji, J. 2016, *ApJ*, 818, 76
- Juhász, A., Benisty, M., Pohl, A., Dullemond, C. P., Dominik, C., & Paardekooper, S.-J. 2015, *MNRAS*, 451, 1147
- Kama, M., Pinilla, P., & Heays, A. N. 2016, *ArXiv e-prints*
- Kley, W., Müller, T. W. A., Kolb, S. M., Benítez-Llambay, P., & Masset, F. 2012, *A&A*, 546, A99
- Kley, W., & Nelson, R. P. 2012, *ARA&A*, 50, 211
- Lacour, S., et al. 2016, *A&A*, 590, A90
- Laughlin, G., & Lissauer, J. J. 2015, *Treatise on Geophysics*, 2nd Edition, 10, 673
- Li, H., Finn, J. M., Lovelace, R. V. E., & Colgate, S. A. 2000, *ApJ*, 533, 1023
- Lin, D. N. C., & Papaloizou, J. C. B. 1993, in *Protostars and Planets III*, ed. E. H. Levy & J. I. Lunine, 749–835
- Lyra, W., Johansen, A., Zsom, A., Klahr, H., & Piskunov, N. 2009, *A&A*, 497, 869
- Lyra, W., Paardekooper, S.-J., & Mac Low, M.-M. 2010, *ApJ*, 715, L68
- Lyra, W., Richert, A. J. W., Boley, A., Turner, N., Mac Low, M.-M., Okuzumi, S., & Flock, M. 2016, *ApJ*, 817, 102
- Masset, F. 2000, *A&AS*, 141, 165
- Mayama, S., et al. 2012a, *ApJ*, 760, L26
- . 2012b, *ApJ*, 760, L26

- Momose, M., et al. 2015, PASJ, 67, 83
- Muto, T., et al. 2012, ApJ, 748, L22
- . 2015, PASJ, 67, 122
- Paardekooper, S.-J., Baruteau, C., & Kley, W. 2011, MNRAS, 410, 293
- Paardekooper, S.-J., & Mellema, G. 2006, A&A, 459, L17
- Papaloizou, J. C. B., & Terquem, C. 2006, Reports on Progress in Physics, 69, 119
- Pérez, L. M., Isella, A., Carpenter, J. M., & Chandler, C. J. 2014a, ApJ, 783, L13
- . 2014b, ApJ, 783, L13
- Picogna, G., & Kley, W. 2015, A&A, 584, A110
- Pinilla, P., et al. 2015, A&A, 584, L4
- Pollack, J. B., Hollenbach, D., Beckwith, S., Simonelli, D. P., Roush, T., & Fong, W. 1994, ApJ, 421, 615
- Qi, C., Öberg, K. I., Andrews, S. M., Wilner, D. J., Bergin, E. A., Hughes, A. M., Hogherheijde, M., & D’Alessio, P. 2015, ApJ, 813, 128
- Quanz, S. P., Amara, A., Meyer, M. R., Kenworthy, M. A., Kasper, M., & Girard, J. H. 2013a, ApJ, 766, L1
- Quanz, S. P., Avenhaus, H., Buenzli, E., Garufi, A., Schmid, H. M., & Wolf, S. 2013b, ApJ, 766, L2
- Rafikov, R. R. 2002, ApJ, 569, 997
- Rapson, V. A., Kastner, J. H., Millar-Blanchaer, M. A., & Dong, R. 2015, ApJ, 815, L26
- Sallum, S., et al. 2015, Nature, 527, 342
- Stauffer, J., et al. 2015, AJ, 149, 130
- Tang, Y.-W., Guilloteau, S., Piétu, V., Dutrey, A., Ohashi, N., & Ho, P. T. P. 2012a, A&A, 547, A84
- . 2012b, A&A, 547, A84
- Tanii, R., et al. 2012, PASJ, 64
- Testi, L., et al. 2014, Protostars and Planets VI, 339
- Thalmann, C., et al. 2010, ApJ, 718, L87

- . 2014, *A&A*, 566, A51
- Turner, N. J., Choukroun, M., Castillo-Rogez, J., & Bryden, G. 2012, *ApJ*, 748, 92
- Udry, S., & Santos, N. C. 2007, *ARA&A*, 45, 397
- van der Marel, N., van Dishoeck, E. F., Bruderer, S., Pérez, L., & Isella, A. 2015, *A&A*, 579, A106
- van der Plas, G., van den Ancker, M. E., Waters, L. B. F. M., & Dominik, C. 2015, *A&A*, 574, A75
- Walsh, C., et al. 2014, *ApJ*, 791, L6
- Ward, W. R. 1997, *Icarus*, 126, 261
- Watanabe, S.-i., & Lin, D. N. C. 2008, *ApJ*, 672, 1183
- Willacy, K., & Langer, W. D. 2000, *ApJ*, 544, 903
- Willson, M., et al. 2016, *ArXiv e-prints*
- Winn, J. N., & Fabrycky, D. C. 2015, *ARA&A*, 53, 409
- Zhang, K., Isella, A., Carpenter, J. M., & Blake, G. A. 2014, *ApJ*, 791, 42